Computational Materials Science 249 (2025) 113565

Contents lists available at ScienceDirect

Computational Materials Science

journal homepage: www.elsevier.com/locate/commatsci

Full length article

A surrogate multiscale model for the design of high entropy alloys

David Gonzalez, Eugene Pavlov, Stefano Valvano *,[1], Angelo Maligno

University of Derby, Institute for Innovation in Sustainable Engineering, Lonsdale House, Quaker Way, Derby, DE1 3HD, United Kingdom

ARTICLE INFO

Keywords:
High entropy alloy
Crystal plasticity
Stacking fault energy
Atomistic modelling

ABSTRACT

We propose a multi-scale physically-based model, for estimating the mechanical properties of a multicomponent alloy by statistically bridging the atomistic (10^{-9}–10^{-7} m), dislocation (10^{-8}–10^{-6} m) and macro (10^{-6}–10^{-3} m) length scales. We propose a temperature and strain-rate dependent dislocation theory model in which the velocity of dislocations is controlled by the average distance between barriers for dislocation glide i.e. the mean free path. The mean free path depends on the estimated distance between lattice distortions employing an atomistic model, and on the evolving immobile dislocation density as calculated by a modified Kocks–Mecking model, in which the mobility of dislocations is determined by the material stacking fault energy. The calculated flow curves and dislocation densities show good agreement with experimental data. The model relies on physically-based equations and parameters coherent with the literature, without empirical parameters, thus holding potential to speed up the pre-design phase of High Entropy Alloys for aerospace and nuclear components.

1. Introduction

1.1. Design of high entropy alloys

Since the 2000s, many exceptional properties of High Entropy Alloy (HEA) such as fatigue resistance [1], excellent strength/high hardness [2], fracture toughness [3], high chemical [4] and heat resistance [5], thermal stability [6], and electromagnetic properties [7] have been the subject of increased attention. Nohring and Curtin [8] indicated that mixing of slightly different atomic sizes leads to distortion in the HEA lattice and slows dislocation activity. This results in increased strength and ductility and promotes the formation and stability of HEA solid solution phases. The lattice distortion results in lattice resistance to the sliding of dislocations, which leads to strengthening of the solid solution, and plays an important role in increasing the yield strength of HEA. Such unique properties of HEA provide a very wide range of applications for aerospace [9], cryogenic [10], nuclear industry [11]. This rises the interest and challenges in HEA alloy design for the development of new HEA with desired properties.

The basic principle behind HEAs is that solid-solution phases are relatively stabilized by their significantly high entropy of mixing compared to intermetallic compounds [12]. In order to understand the unique properties of HEA, in 2012 [13] did the first prediction of solid-solutions phases and estimated the possible crystal structures for HEAs. In 2016, the work of [14] underlined the importance of the entropy conditions in the design of High Entropy Alloys. In order to develop a systematic procedure to study this class of materials, it is mandatory to consider their multicomponent nature. Being multicomponent, HEA alloys have a wide palette of constituent elements, and in situation, where possible alloy compositions are not limited by equiatomic ratios, millions of unique alloy compositions are possible. Naturally, the study of such a vast compositional space of the HEA system and predicting its properties by trial and error, without a complex, physic-based methodology, looks unpromising.

The main objective of this research is to aid the design stage of HEAs by using a ICME framework for predicting the material properties from its atomistic (10^{-9}–10^{-7} m), and dislocation configurations (10^{-8}–10^{-6} m). Integrated computational materials engineering (ICME) is an emerging multi-disciplinary field that aims to establish causal relationships between the material multi-scale structure and properties.

The solution to this important materials science problem lies in the development of a physical approach, the basis of which is a multi-scale model that allows combining the experimental database of materials science and computer simulation methods. This kind of methodology would significantly reduce the time and improve the quality of HEA design [12]. Their four core effects A. Rempel (2020) A. Rogachev (2020): high entropy, sluggish diffusion, severe lattice distortion, and cocktail effects have been reviewed to facilitate the alloy design strategies for suitable compositions and processes in industrial applications Yeh (2013).

* Corresponding author.
E-mail address: s.valvano@derby.ac.uk (S. Valvano).
[1] Associate Professor in Integrated Computational Materials Engineering.

https://doi.org/10.1016/j.commatsci.2024.113565
Received 16 March 2024; Received in revised form 14 November 2024; Accepted 22 November 2024
Available online 21 December 2024

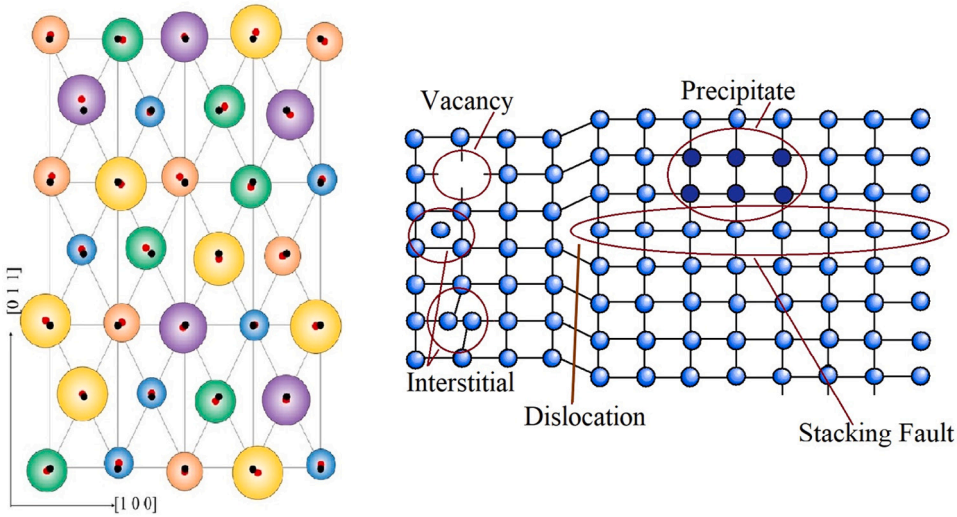

Fig. 1. Possible barriers for dislocation motion due to lattice energy changes arising from lattice distortions (left), dislocation defects (right).

The wide range of properties in HEA have led to employing various traditional modelling techniques, including Molecular Dynamics, Monte Carlo, DFT and *ab initio* methods, statistical physics and dislocation theory. Recently, new methods have appeared in materials science, designed for the rapid assessment of the multidimensional compositional space of HEA alloys. In particular, artificial intelligence methods such as neural network [15], data mining, cluster analysis, principal component analysis [16] and statistical analysis [17] also have been proposed.

1.2. The bridge between scales

In general, the multiscale study and evaluation of the properties of complex materials involves the use of atomistic models. Regarding the HEAs design, it is possible to find in the open literature many papers devoted to the application of atomistic technique combined with a thermodynamic calculations [18], using Monte-Carlo (MC) [19], or considering first-principles density functional theory (DFT) [20] and molecular dynamic (MD) simulations. Unlike the DFT method, molecular dynamics (MD) strongly depend on the inter-atomic potentials, but considerably more flexible to capture temperature and micro-structure effects of nanostructured systems than their DFT counterpart. It is possible to find in the literature multiscale methods, which involve the modification of the atoms motion equations coupled with the mechanical material characteristics for a direct description properties at high scale level [21]. In order to understand how to set-up equations in the multiscale methods, it is important to have an overview of the possible dislocations mechanisms, see Fig. 1. In the left part of Fig. 1 the red dots stand for the equilibrium atomic positions in a bcc solid-solution alloy with lattice distortion, while the black dots stand for the ideal positions in an undistorted lattice. The schematic corresponds to a projection view along the $[0\bar{1}1]$ direction. The big solid circles in different colours represent individual types of atoms in the alloy [22]. In the right part of Fig. 1 shown possible types of crystal structure defects. As far as we know, modelling of mechanical properties for HEA is defined by theoretical concepts about plasticity [23,24]. The derivation of meso and macro flow curves for different temperatures, strain rates etc., in function of pure atomistic models is still difficult in practice and it demands coupling with wide set of macroscopic properties. On the other end, the use of purely empirical approaches to predict plasticity, such as the Johnson–Cook model, relies on many arbitrarily chosen parameters lacking capability for extrapolation.

There is a need for a bottom-up scale approach that can capture the key deformation mechanisms at lower scales to derive the proper macroscopic behaviour. Such model also should be able to predict deformation at different strain rates and temperatures relevant to manufacturing and service conditions, without any arbitrarily chosen adjustable parameters. In this article we propose a practical combination of two approaches that allows to obtain the flow curves, dislocation density and mean free path evolutions depending on various conditions: strain rates, temperatures, concentration, etc. This multi scalable approach is using an interatomic potential model at the lowest level, and dislocation theory at meso scale level, in order to derive the mechanical properties of HEA alloys at the macro scale. The mean free path is a characteristic distance that plays a key role in plasticity, because it determines the likelihood of a gliding dislocation to encounter obstacles in its movement such as subgrains, grain boundaries or precipitates in various metallic alloys (e.g. [25]). In our article, it is assumed that the mean free path reduction is due to the local atomic energy barriers related to lattice distortion in HEAs. We derive the mean free path distance from the results of an stochastic atomic model of random HEA alloy. In our calculation of the evolving mean free path, we also consider the evolution of the dislocation density, which generally increases with strain and further hinders dislocation movement. Thermally activated processes are particularly relevant for the design of alloys for advanced nuclear applications, where HEAs have showed promise [26]. For example, during irradiation damage in nuclear materials, where the evolution of dislocation loops play key role, the change of slip system of the screw component of the dislocation loop requires dislocation climb [27]. This can impact the performance under service conditions, since dislocation climb requires diffusion to occurs and diffusion is know to be sluggish in HEAs due to lattice distortions. For thermal activated processes, such as dislocation climb which requires diffusion, we assume an Arrhenius relationship, whereas for dislocation glide, we assume that the motion is controlled by the mean free path. We further include the effect of the material stacking fault energy, which plays a crucial role in deformation and will be explained in more detail in later sections.

2. The atomistic model

During crystallization from the melt, the atoms of the HEA are packed into simple crystalline structures, where atoms of different types are located randomly in the lattice nodes. In this case, from the point of view of the classical theory of alloys, the HEA is a disordered substitution solid solution. This means applying tools of classic metal alloy theory for calculating the configuration entropy term in Eq. (1)

of such an multi-component alloy would become an insurmountable problem.

This process would involve: (1) introducing order parameters (Short Range Order, SRO, and Long Range Order, LRO) which are related to probabilities P_n in Eq. (1), (2) derivation of free energy of Eq. (1) by order parameters and (3) finding the equilibrium values of order parameters solving the system of non-linear equations. Even for only two components alloy. this process becomes already a very tedious mathematical process.

For this reason, we propose a model where we calculate all the possible atomic configurations (e.g. Ni-Ni, Ni-Fe, etc.) using pair potentials. Then we estimate the distribution of the energy of the alloy using a random positioning of the atoms in the lattice, considering the possible configurations up to the 3rd coordination sphere. In the next subsections, we introduce (1) the methodology that would be required to solve for the configuration entropy problem (not employed here), and (2) we describe the proposed random alloy model in more detail.

2.1. Configuration entropy of HEA solid solution

The temperature-concentration dependencies of the physical properties of ordering alloy are determined by changes in the order parameters included in the entropy term of the free energy Eq. (1). Recent experimental studies have shown the presence of SRO in various HEA samples [28,29]. However, the interpretation of direct experiments to determine the short-range order parameters in HEA alloys remains a difficult task due to the temperature effect of lattice distortion, which leads to an anomalous decrease in peak heights. The difficulty results from resolving the spatial extent of the ordering when averaging over a large region of material and the diffusive nature of the local ordering [30]. It is worth to be noted, in the case of a multicomponent HEA taking into account the calculation of the equilibrium entropy S, the theoretical approach became extremely complicated. This can be said about applying of any methods, that are used for this problem, such as the method of concentration waves [31], the theory of ordering of solid solutions [32], and most widely used the cluster expansion method [7]. For example, the serial fit of cluster expansion in multicomponent crystalline solids, need many terms and at the same time, the number of terms grows rapidly with the diameter of the cluster. As additional terms are added, the series coefficients may converge poorly given limited number of configurations [7]. As rightly noted in [11], the calculation of the entropy configuration in the case of an HEA alloy became difficult even due to the interpretation of temperature (difficulties is that associated with evaluating the influence of the entropic term on the Gibbs free energies of solid solutions). In a broad sense, the entropy and number of elements factor, which is believed to underlie the mechanical properties of HEA alloys, remains an area of active research and debate. For example, according to [3,33], high entropy configuration allows an ex post explanation of why a solid solution forms, but it is unhelpful as a priori predictor of thermodynamic stability and a clear dependence of mechanical properties on the number of elements [34].

The main feature of HEAs is the formation of a single-phase thermodynamically stable substitutional solid solution, often fcc or bcc lattices [35]. However, interactions of solute components provide thermodynamic driving force for the non-random occupation of atomic positions. It leads to arise ordering in the nearest surroundings of alloy atoms. By minimizing the entropy of the free energy of the alloy by the probabilities of filling the lattice sites, it is possible to describe the most probable structures of the alloy.

The statistical thermodynamic approach for solid solutions [31,32] uses a complete description of such ordering, taking into account its structural and concentration characteristics. The definition of the free energy of a solid solution alloy, which depends on the value of the radius vectors of the alloy atoms $\vec{r}_i$, can be written as [30,31,36,37]:

$$F = U(V(\vec{r}_1), V(\vec{r}_2)...V(\vec{r}_n)) - k_B \cdot ln(W(P_1(\vec{r}_1), P_2(\vec{r}_2), \dots, P_n(\vec{r}_n))) \cdot T \quad (1)$$

where first term $U(\vec{r}_1, \vec{r}_2...\vec{r}_n)$ is the energy of alloy. The term $S = k_B \cdot ln(W(P_1(\vec{r}_1), P_2(\vec{r}_2), \dots, P_n(\vec{r}_n)))$ is the configuration entropy of the alloy, where W is the statistical weight, and $P_n(\vec{r}_n)$ is the probability of the crystal lattice nodes occupation [30,31,36].

Pair interatomic potentials $V_A(\vec{r}_A)$, $V_B(\vec{r}_B)$ and $V_{AB}(\vec{r}_{AB})$ of (two) component A and B alloy, define the energy of the alloy $U(V(\vec{r}_1), V(\vec{r}_2)...V(\vec{r}_n))$ [7,19]. Different type of pair potentials can be obtained directly from *ab initio* calculations [38,39], or fitting experimental data in case of model potentials, such as Leonard-Jones potential [40], Mie potential and Morse potential [41,42]. Pair potentials of mixed components V_{AB} can be calculated using the Lorentz–Berthelot rules [40] or other rules [43].

In our study, we do not consider configuration entropy of the alloy at the atomic level, see Eq. (1). Instead, we take into consideration all changes associated with alloy structure and temperature indirectly, within the framework of the dislocation theory. For calculation, we use only the energy of the alloy as its basic characteristic at the lowest level of consideration, which does not depend on temperature. Although it does not allow us to completely determine the ordering conditions and structural features at the atomic level, the transition to a continuum level makes possible to describe a wider range of physical phenomena affecting mechanical properties, such as the decomposition of a solid solution and the presence of precipitates and inter-metallic phases [44–47], that is impossible within the atomistic approach.

2.2. Random alloy model

Since we do not consider the configuration part of entropy and the ordering associated with it, we adopt a simplified model that assumes random filling of lattice nodes. The potential energy of structure per atom in random alloy model can be written [7,19]:

$$U(\vec{r}_1, \vec{r}_2...\vec{r}_n) = \frac{1}{2}\sum_{i=1}^{I} M_i \sum_{\alpha\beta} P_{\alpha\beta} V_{\alpha\beta}(|\vec{r}|) \quad (2)$$

where M_i is number of atoms in the ith coordination sphere. The probability of occupation of any individual lattice node by a type solute is proportional to concentration alloy component C:

$$\sum_{\beta} P_{\alpha\beta} = C_\alpha \quad (3)$$

In this model, we do not take into account the effect of temperature on the energy of the alloy, since the pair potentials $V_{\alpha\beta}(\vec{r}_{\alpha\beta})$ are assumed to be independent of temperature. Such accounting requires additional assumptions [42]. An example of the pair interaction and the relationship between the energy barriers and the free path dislocations is given in Fig. 2. An important parameter of the calculation by the formula Eq. (2) is the distance between of the nearest atoms $|\vec{r}_{ij}|$, which is proportional to the lattice parameter $a_{lattice}$. Lattice distortions in the HEA affect the value of the lattice parameter, as shown in [48], up to 5%. This affects the alloy energy estimation, which can also vary slightly. In the calculations based on Eq. (2) we used the value of lattice parameter [49] and Morse type pair potentials [42] which are short-range, see Fig. 3. These potentials rapidly decay after the second coordination sphere and do not have spatial orientation of the bond. To obtain the potentials of mixed components (e.g. Fe-Ni) in the case of a HEA alloy, we used combination rules [43]. In the random alloy model, described in Eq. (2), instead of a single value of the alloy energy, we get this Gaussian distribution, whose characteristics are associated with the possible atomic configurations in the alloy, an example is given in Fig. 1.

In our random alloy model, we use the pair-potentials (see Fig. 3) to calculate the energy of nodal position in the lattice up to the 3rd

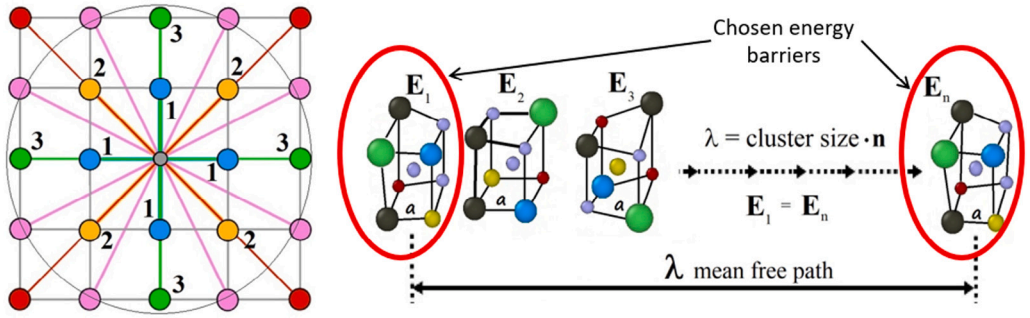

Fig. 2. Left: Square 2D lattice with effective pair interaction highlighted. Equivalent interacted pairs (same distance)correspond to the 1st (blue), 2nd (yellow), 3rd (green), 4th (pink) and 5th (red) neighbours respectively. Right: Schematic representation of the mean free path distance between selected energies of lattice clusters.

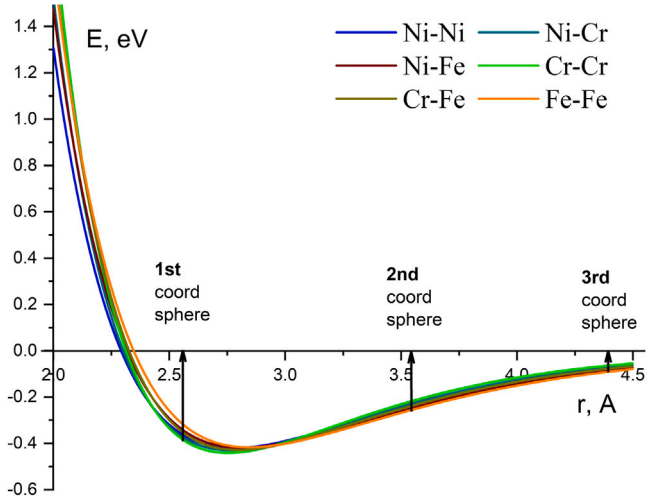

Fig. 3. Pure [42] and mixed [43] Morse potentials of alloy component. The positions of the first three coordination spheres are marked by arrows.

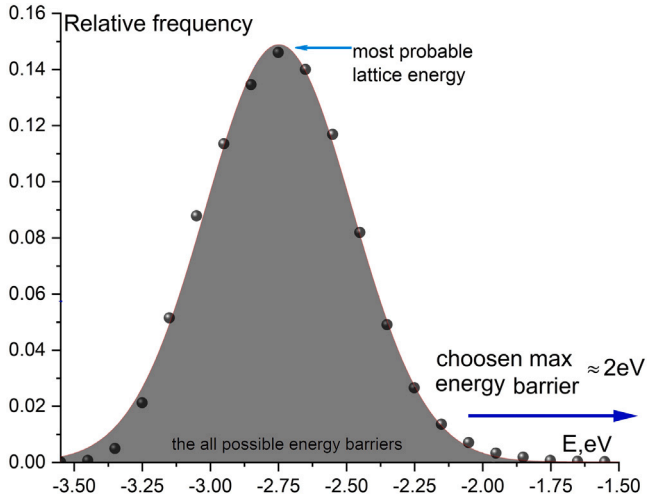

Fig. 4. The distribution of energies values of local lattice configurations in the FeCoCrNi HEA alloy calculated by the random alloy model. This distribution lays within the energy range of typical structural defects; such as dislocation energy [50–54], dislocation core energy [53], dislocation interaction energy and dislocation slip energy [55], dislocation kink energy [23,56], cross-slip activation energy [8], SFE energy [57], and diffusion energy [58–60].

coordination sphere (see left Fig. 2). The results of these calculated energies are shown as data points in Fig. 4. More details will be given in the results section. To obtain the Gaussian distribution we will use the method described by [8] :

$$P(E_{act}) = A \cdot \int_{-\infty}^{E_{act}} e^{-\frac{1}{2}\cdot\frac{(E+E_{avg})^2}{w_0}}\, dE = \frac{1}{N} \tag{4}$$

where N represents the number of segments between barriers,against dislocation motion, along a long dislocation [8]. The compositional disorder in random multi-component alloys leads to local changes in interatomic distances and corresponding changes in lattice configuration energies. The fluctuations of interatomic distances, and their associated lattice configuration energies, in multicomponent alloys have been studied by means of Monte Carlo simulations containing 2000 atoms [48], and by the Embedded Atom Method (EAM) [8]. These local energies changes would result in a heterogeneous effective mean free path. We do not consider these it is beyond the scope of our study. In our work, we are interested in the averaged macroscopic mechanical properties, and therefore use the averaged mean free path.

The Gaussian distribution in Fig. 4 is characterized by the distribution parameters A, E_{avg}, w_0. Following the logic in [8] and Eq. (4), we can estimate the averaged distance between energy barriers due to local lattice distortions in our HEA alloy. The distance between barriers d is related to the size of the atomic cluster L, with energy E_{act} divided by the probability $P(E)$ gives us the distance between these atomic configurations previously calculated with formula (2):

$$\lambda_{lattice} = \frac{L}{A \cdot \int_{-\infty}^{E_{act}} e^{-\frac{1}{2}\cdot\frac{(E+E_{avg})^2}{w_0}}\, dE} \tag{5}$$

The distribution in Fig. 4 represents a set of possible values of the energies of FeCoCrNi HEA alloy, which magnitudes can be correlated with various types of spatial defects in the crystal lattice. In order to calculate this distance, $\lambda_{lattice}$, from Eq. (5) we only need to choose one integration parameter E_{act}, since every other parameter has already been calculated in our model.

3. Dislocation theory model

Multiple crystal plasticity finite element models (CPFEM) have been used to describe plastic deformation in viscoplastic materials for a range of metallic alloys. CPFEM models rely on (1) the material constitutive equations at the grain level and (2) building a Representative Volume Element (RVE) of grains to study local plastic effects, such as strain localization between grains. To cite a few of many, these CPFEM models have been employed to study intergranular stresses [61,62], deformation twinning [63], high temperature deformation [64–66], grain boundary stress [67–69], fatigue crack initiation [70], fatigue crack propagation [71], void growth [72], strain path changes [73–75] and the effect of precipitates [76]. CPFEM can also be employed to study the effect of grain morphologies on deformation following additive manufacturing [77,78]. This can further contribute to the

design of tailored micro-structures for optimum mechanical performance, through varying process parameters (e.g. power, build speed and path) in increasingly emerging techniques such as additive manufacturing [79]. Here, we focus only on the physically-based constitutive equations to describe the plasticity at the crystal level because our aim is the design of HEAs based on the mechanical macroscopic properties, rather than investigating local plasticity effects. Physically-based approaches for various metal alloys, without the requirement of finite elements, have been used to successfully predict deformation [80,81], creep damage [82,83] or particle size distributions in precipitation-strengthened alloys [84]. A CPFEM version of our proposed model can by readily built by incorporating these equations at the crystal level and building a RVE, as per the previously cited CPFEM studies. We obtain the averaged behaviour of the entire polycrystalline material via the Taylor factor, m, which is a common practice. For randomly oriented face-centred and body-centred cubic metals, $m \approx 3$. The goal is transforming the global stress into the shear stress in the local crystal system. This approach relies on averaging the stress over the grains and considering the most-favoured slip systems.

In order to develop a new multi-scale approach capable of identifying conditions for optimal design for HEAs, it is necessary to establish the material constitutive equations. These are briefly described here and detailed in the next sections. The velocity of a dislocation is influenced by the applied stress, temperature and the microstructure. We propose a viscoplastic strain-rate and temperature dependent model, where the dislocation density evolution is given by [85]. In our approach, the temperature dependency is controlled by the thermally activated deformation via Arrhenius expression. We further consider the tendency for cross-slip, associated to the SFE-dependency on temperature. This approach can be applied for any metal beyond HEAs, as long as the SFE-dependencies on temperatures and mean free path distances are experimentally known or reasonably estimated. In high SFE metals, dislocation glide is promoted, due to the lack of strong stacking fault barriers. Here, we focus on cross-slip the mechanism because it plays an important role in the evolution of work hardening and dislocation structuring in metals [8]. Other mechanisms are also SFE-dependent, such as dislocation climb or dynamic recovery leading to faster rearrangement and annihilation of dislocations. However, these are already taken into account via the thermally activated velocity of dislocations in Eq. (7). We use the estimation of lattice mean free path estimations, $\lambda_{lattice}$, calculated from the atomistic model presented in earlier sections, to feed into the dislocation mean free path estimated from the dislocation density. The SFE is the most crucial intrinsic property to determine the deformation mechanism and to optimize the mechanical properties of FCC HEAs. When designing HEAs, it is crucial to know the SFE. In our work, we take the SFE and elastic properties of the studied FeCoCrNi alloy from experimental observations [86]. However, these material properties can be predicted from models based on first principles [87] and data-driven machine learning [88], bringing further promise for the design stage of HEA.

3.1. Physically-based viscoplastic model

The relationship between flow stress, temperature, and applied strain rate is influenced by the energy required for dislocations to overcome barriers during slip. The size of these energy barriers determines the dependence of flow stress on temperature and strain rate. An applied resolved shear stress τ produces a force τb per unit length of the dislocation line. Let the spacing of the obstacles along the line be l, so that the applied forward force on the line per obstacle is τbl. Then, the mechanical work when moving the dislocation a distance d via thermal activation is τdbl. The activation volume has been proposed phenomenologically as $V^* = dbl$ [89]. By taking the distance swept by the dislocation, d, as the magnitude of the Burger's vector, b, the activation volume becomes $V^* = lb^2$ and the mechanical work becomes τV^*. In this context, the Helmholtz free energy change is the isothermal energy change to overcome an obstacle. This is the total energy required to move the dislocation, but part of this energy is provided in the form of mechanical work done by the applied load on the dislocation line. Therefore, the Gibbs free energy change between two states at the same temperature and applied stress is:

$$\Delta G = \Delta F - \tau V^* \tag{6}$$

where ΔF is the Helmholtz free energy change and τ is the net stress acting on the dislocation (see for example [90]). When considering the activation energy for dislocation motion in metals, the entropy term is generally believed to be relatively small compared to the enthalpy term and it is common to simplify the equation by neglecting the entropy term [91–93], thus $\Delta G \approx \Delta H$. Additionally, the Helmholtz free energy is associated with the total activation energy, Q, required for the dislocation mechanism to occur e.g. dislocation glide climb or kink [94]. Thus Eq. (6) becomes:

$$\Delta H = Q - \tau V^* \tag{7}$$

where ΔH is the free enthalpy for dislocation motion associated with thermal fluctuations and τV^* is the work carried out by the stress field. The probability of energy ΔH occurring by thermal fluctuations at temperature T is given by the Boltzmann factor $exp(-\Delta H/kT)$, where k_B is the Boltzmann constant. The dislocation is effectively vibrating at the atomic frequency, or the Debye frequency, [95]. Assuming the distance moved for each obstacle overcome is the magnitude of the Burgers vector, the velocity of the dislocation, v, will be determined by the rate at which the dislocation successfully overcomes barriers as:

$$v = b\nu_D exp\left(\frac{-\Delta H(\tau)}{K_b T}\right) \tag{8}$$

The movement of a dislocation is often hindered by obstacles in the lattice. Overcoming an obstacle often requires dislocation climb, which requires interstitial diffusion to occur. Climbing and diffusion are promoted at high temperatures and hence the proposed relationship between dislocation velocity and temperature via Arrhenius equation. When substituting Eq. (7) into Eq. (8) it is possible to obtain:

$$v = b\nu_D exp\left(\frac{\tau V^* - Q}{K_b T}\right) \tag{9}$$

The exponential term in Eq. (9) has been proposed to be also proportional to the velocity of glide of jogged dislocations [96], thermally activated unpinning of dislocations [97], as well as for thermally activated dislocation glide [98], kink and jog motion [99,100]. In the former, jog segments act as pinning points for dislocation motion, involving a combination of dislocation glide and climb, where the pinning distance between dislocation jog segments (i.e. mean free path) control the dislocation motion. For all these mechanisms, plastic slip is assumed to be driven by the resolved shear stress on the slip system. The effective stress in Eq. (9) is defined by:

$$\tau = \tau_{applied} - \tau_{drag} - \tau_{forest} \tag{10}$$

where $\tau_{applied}$ and τ_{drag} are the applied and drag stress associated with the internal stresses arising from obstacles. The shear stress required to overcome forest dislocations in secondary slip systems is determined by τ_{forest}. The drag shear stress is the controlling mechanism for glide i.e. the larger this distance the easier the dislocation glide. The shear stress for dislocation glide through an array of obstacles was proposed as [101]:

$$\tau_{drag} = \beta\frac{Gb}{\lambda} \tag{11}$$

where G is the shear modulus, λ is the mean free path and β is a dimensionless constant, $0 \leq \beta \leq 1$ [102] determining the average strength of the pinning points. By using the Taylor flow stress equation (substituting $\lambda = \sqrt{(}\rho_{fo})$ in Eq. (11)), β has been estimated as ≈0.3 [103]. Theoretical and experimental studies in F.C.C crystals,

suggest that $\beta \approx 0.35 \pm 0.15$ for forest dislocation junctions [104]. This expression has been the basis for multiple studies thereafter, such as an early computational study on the movement of dislocations loops through arrays of obstacles, which is relevant to irradiation hardening [105]. We use this approach to calculate the stress resistance by forest dislocations to calculate τ_{forest} by considering the evolution of the calculated forest dislocation population. According to the Orowan relationship, the equation for shear strain rate is proportional to the velocity for dislocation glide:

$$\dot{\gamma} = \rho_{mo} \cdot v \cdot b \tag{12}$$

where b is the Burger's vector magnitude and ρ_{mo} is the mobile dislocation density. A Taylor constant M = 3, has been used accordingly to relate both sets of coordinates ($\dot{\epsilon} = \dot{\gamma}/M$; $\sigma = M\tau$). Although alternative constitutive equations for plasticity are possible, our focus is to integrate; (1) the effect of dislocation barriers arising from lattice distortions in HEAs (2) the dislocation density evolution on the mean free path distance between dislocations and, (3) the effect of the stacking fault energy on deformation. This will be covered in the next sections.

3.2. Dislocation density evolution

As plastic deformation takes place, there exists a competition between work hardening (associated with the storage of dislocations) and work softening (associated with the annihilation of dislocations). In 1953, Cottrell described work hardening as a 'spectacular phenomenon' and remarked that 'this was the first problem to be attempted by dislocation theory and may be the last to be solved' [106]. Despite work hardening being a major subject of research efforts and discussions at international conferences in the 1950s and 1960s, we are far from a unified theory to fully explain it [107]. Kocks and Mecking [85] proposed a model, the Kocks–Mecking (K–M), to capture the evolution of the immobile dislocation density (see also [108]). This model was first extended to capture the strain-rate and temperature dependencies, being able to convert stress–strain data into creep curves without any adjustable parameters [109]. In our approach, we propose a modified K–M viscoplastic strain-rate and temperature dependent model, controlled by the SFE-dependency on temperature (as shown later), where the immobile dislocation density evolution was expressed by the K–M model as:

$$d\rho_{im} = (A \cdot \sqrt{\rho_{im}} - B \cdot \rho_{im}) d\gamma \tag{13}$$

where A and B are parameters associated to the generation and annihilation of dislocations respectively. The term ρ_{im} represents the immobile dislocation density. Only some dislocations are mobile and thus contribute to plastic deformation. Dislocation on secondary slip systems or forest dislocations can also hinder plastic deformation, effectively acting as immobile. However, as seen earlier, forest dislocations are treated as a population of dislocations that give rise to a lattice resistance stress and thus not included within the immobile dislocation density due to the more complex nature of interactions such as jogged dislocations. The immobile dislocation density represents dislocation populations that can pin movement in the primary slip plane. This includes dislocation tangles, stacking faults or other interactions with Shockley partial dislocations, such as stair-rod [110] or Lomer–Cottrell locks [111,112]. The overall total dislocation density, across all slip systems, is thus defined as:

$$\rho_{to} = \rho_{im} + \rho_{mo} \tag{14}$$

where ρ_{to}, ρ_{im} and ρ_{mo} are the total, immobile and mobile dislocation densities respectively. Our model is based on the work of Kubin and Estrin [113] who first proposed to introduce two dislocation densities in their model: the immobile and the mobile. As for the dislocation character, some of the multiple proposed material constitutive models in the literature can distinguish the evolution of screw and edge dislocation components of the dislocation density [71,114]. Here, we consider the bulk dislocation density only, firstly for simplicity and secondly, for the difficulty associated to experimentally validate the screw and edge component populations.

The dislocation densities described in the above equations, ρ_{to}, ρ_{im}, ρ_{mo}, refer to the dislocations contained in the bulk of the material i.e. across all slip systems. In dislocation theory, latent slip systems have traditionally been referred to as slip systems different to the primary slip system where plastic deformation is being studied. Mobile and immobile dislocations on latent (or secondary) slip systems are considered forest dislocations that can act as obstacles. Therefore, only the mobile dislocations on the primary slip system contribute to deformation (12). The relationship between the mobile dislocation density in a single slip system and the bulk mobile bulk dislocation density, α, will be:

$$\rho^{\alpha}_{mo} = \frac{\rho_{mo}}{n} \tag{15}$$

with n being the total number of slip systems. Similarly, the forest dislocations hinder plasticity and include the immobile dislocations contained in the primary slip system and the total dislocation density in other (secondary) slip systems. Since we are using the Taylor factor to transform local to global coordinate systems, we assume that all slip systems have the same dislocation densities. The forest dislocation density is therefore defined as:

$$\rho_{fo} = (n-1)\rho^{\alpha}_{to} + \rho^{\alpha}_{im} \tag{16}$$

where ρ^{α}_{to} and ρ^{α}_{im} represent the total and immobile dislocation density in slip system α. Although the proposed model statistically aims to capture the effect of forest dislocations, it is important to recognize that the details of these interactions can be complex. For example, a gliding dislocation that finds another jogged dislocation, where at least one of the two dislocations has screw character, is a thermally activated process that requires stress [111].

3.3. Dislocation mobility dependency on the stacking fault energy

It is essentially impossible to experimentally determine ratio between mobile and immobile dislocations. This applies for an annealed metal as well as for a heavily deformation metal. As the mobility of dislocations is also temperature dependent, this ratio is defined in the absence of thermal activation (0 degrees Kelvin). The ratio between mobile and immobile dislocations at the can be conveniently defined as:

$$R = \frac{\rho_{mo}}{\rho_{im}} \tag{17}$$

The mobile dislocation density equals the immobile dislocation density when R = 1. The evolution of the mobile dislocation density with strain was proposed by Barlat et al. [80] as a dependency on the evolution of the dislocation mean free path. This dependency of the dislocation density evolution with the MFP is also present in our model (Eqs. (11), (9) and (13)) The immobile dislocation density has been proposed to be linearly dependent on Stacking Fault Energy [115,116]. This relationship is based on the profound effect that SFE has on plastic deformation [107]. Screw dislocations in materials with high SFE tend to readily cross-slip to different slip planes, facilitating plastic deformation [117]. This can greatly enhance the material ductility and deformation capacity. In materials with high SFE, the shorter distance between two Shockley partial dislocations allows easier association of partial dislocations, which is a geometrical requirement for cross-slip. Conversely, a material with low SFE is associated with an increased tendency for the formation of deformation twins [118] and planar defects such as stacking faults in crystalline materials. Twinning is a common experimentally observed deformation mechanism in materials with low SFE values. In the context of HEAs, twinning has also been attributed to the relatively low stacking fault energy (20–25 mJ/m2)

of a CrMnFeCoNi alloy [3], which is perhaps the most studied HEA alloy at cryogenic temperatures due to its outstanding combination of strength and toughness [119]. In materials with low SFE, dislocations are less likely to cross-slip, and they tend to remain on their original glide planes. This can lead to a higher resistance to plastic deformation and result in materials that are stronger but less ductile. Atomic models [120], supported by creep data of more than thirty metals and alloys [121], suggest a relationship between the strain rate and the SFE as $\dot{\epsilon} \propto (\gamma_{SFE}/Gb)^3$. Argon and co-workers [115,116] have proposed the mobile dislocation density to be proportional to the SFE as $\rho_{mo} \propto \gamma_{SFE}/Gb$. With increasing temperature, b and G have been experimentally observed to slightly increase and decrease respectively in many metals and alloys, including CrMnFeCo alloy [86]. For simplicity, we reasonably assume the changes of the product Gb are small when compared to the change in SFE. Experimentally, it has been observed that SFE increases with temperature for various metallic alloys e.g. [122], [123], including CrMnFeCo [86]. In our approach we assume that the ratio of mobility increases linearly with the increasing SFE. Based on the above, we define the ratio of the dislocation mobility as:

$$\frac{\gamma_{SFE}}{\gamma_0} = \frac{\rho_{mo}}{\rho_{im}} \tag{18}$$

where $\gamma^0{}_{SFE}$ is the stacking fault energy at $0K$ and γ_{SFE} is the stacking fault energy at the actual temperature of the material. It should be noted that, while this linear expression aims to reasonably capture the overall effect of the SFE on the mobility of dislocations, other more complex relationships between dislocation mobility and SFE may be needed to describe hardening, particularly during recovery. For example, mobile dislocations, which motion is SFE-dependent, can unlock Lomer–Cottrell locks in stage III hardening or annihilate Orowan loops and edge dislocations (via dipole trapping) in Stage IV hardening [112]. Combining (14) and (18), we obtain a relationship of the evolution of immobile dislocations as a function of the total dislocation density:

$$\rho_{im} = \frac{\rho_{total}}{1 + R\frac{\gamma_{SFE}}{\gamma^0{}_{SFE}}} \tag{19}$$

The SFE for the CoCrNiFe alloy has been estimated to be $\gamma_{SFE}^{77K} = 13\ \mathrm{mJ/m^2}$ and $\gamma_{SFE}^{293K} = 32.5\ \mathrm{mJ/m^2}$ at 77 K and 293 K respectively, by means of neutron diffraction [86]. Observations and estimations of SFE suggest that, at least for a large temperature range, there is approximately a linear relationship between SFE and temperature. Assuming that this is valid for the temperatures being considered here, the SFE increases linearly with temperature and the calculated SFE at 0 degrees Kelvin is $\gamma^0_{SFE} = 6\ \mathrm{mJ/m^2}$ for this alloy.

The choice of the R ratio is not trivial due to the lack of direct experimental data to quantify it. However, it is well accepted that the dislocation mobility is higher in the grain interiors that near the grain boundaries, as the latter act as barriers for dislocation storage such as pile-up dislocations. Additionally, while a grain deforms predominantly by single slip in the grain interiors, strain gradient theory [103] and its first numerical implementation using finite elements [124], have been used to support the hardening by geometrically necessary dislocations near grain boundaries [125,126]. Finite element crystal plasticity studies in copper at room temperature, which also has a FCC crystal structure, found the chosen R ratios (0.05 and 0.33) to have a profound effect on the evolution of geometrically dislocations during cyclic fatigue [127]. In another crystal plasticity study of deformation at very high strain rates ($\approx 10^5\ \mathrm{s^{-1}}$) in copper and aluminium [128], $\rho_{im} = \rho_{mo}$ was chosen at 300 K. As we define R at 0 K in Eq. (17), we substitute the corresponding approximated stacking fault energies in Eq. (19), giving $R \approx 0.5$ at 0 K. Although the arbitrarily chosen values of the mobile to immobile dislocation density ratio are low (R < 1) in these studies, it is reasonable to expect the dislocation mobility of dislocations will be higher (and higher value of R) at strain rates of $\approx 10^{-4}$–$10^{-3}\ \mathrm{s^{-1}}$ and away from microstructural heterogenities such as grain boundaries. Note that the above proposed approach is only valid for comparing dislocation mobilities of alike crystal structures, as FCC metals have relatively high dislocation mobility because of the existence of multi-slip systems, as opposed to HCP crystals that tend to twin more often.

3.4. The role of mean free path on dislocation motion

As introduced earlier, the advancement of dislocations is hindered by forest dislocations. The mean free path (MFP) represents the average distance between pinning points as the dislocation advances through the lattice. The MFP, when using Kocks–Mecking model, λ_{KM}, is related to the current immobile dislocation density. Combining the Taylor equation $\tau = \beta Gb\sqrt{\rho_{im}}$ and Eq. (11) one obtains :

$$\lambda_{KM} = \frac{1}{\sqrt{\rho_{im}}} \tag{20}$$

Note that the higher the immobile dislocation density, the lower the MFP, and the easier a dislocation can slip through the lattice as the pinning points are more far apart. However, the dislocation movement is not only hindered by immobile dislocations but also by local energy barriers, as described in previous sections using the atomistic approach. We introduce this average distance between high energy barriers as $\lambda_{lattice}$. The inverse of the mean free path of a moving dislocation has been proposed as the summation of the inverses of characteristic distances that contribute to hardening in nickel super-alloys i.e. grain size, sub-grain size and average distance between precipitates [25]. The combined MFP of the lattice energy barriers plus the average dislocation distance is thus defined as:

$$\frac{1}{\lambda} = \frac{1}{\lambda_{KM}} + \frac{1}{\lambda_{lattice}} \tag{21}$$

where the smaller distance controls the combined distance.

4. Results of the combined atomistic-microscale model

4.1. Calculation of the mean free path by the atomistic model

To estimate the distance between the barriers, we obtained the probability distribution (Fig. 4) for all possible lattice energy values. We calculated the energy up to the third coordination sphere in the summation in Eq. (2). As the calculation results show, taking into account the summation of higher coordination spheres slightly shifts the peak to the left, since the pair potentials included in the summation rapidly decay with distance. Then, the array of possible lattice energy values was used for statistical analysis. As shown by the statistical sampling results, this energy distribution is accurately described by the Gaussian distribution in Fig. 1. We fitted this energy distribution for the FeCoCrNi alloy using the Gaussian distribution parameters $A = 0.1488, E_{avg} = 2.748, w_0 = 0.27$. These parameters are determined by the current values of the pair interatomic potentials $V_{\alpha\beta}$ (in this case the Morse potential of Benassi (2018) was used), and the value of crystal lattice parameter $a_{lattice}$ was taken from [129].

The position of the distribution peak and its halfwidth are significantly affected by the parameters of the potentials, primarily the depth of the interaction energy, which is ≈–0.4 eV in 3 or parameter D in [42]. Next, we compare our results with previously reported ones. First estimations of maximum possible cohesive energy of pure components alloys were made in 1954, and can be found in the monograph [130]. Recent estimations for this HEA alloy are around 3 eV [131]. The peak of our energy distribution coherent with these theoretical and experimental estimations. In order to calculate the mechanical properties of the alloy, we need to describe the constitutive laws for plasticity which rely on dislocation motion. Dislocation motion is hindered by barriers in the crystal bulk and the characteristic distance between obstacles, or mean free path, plays a key role. This

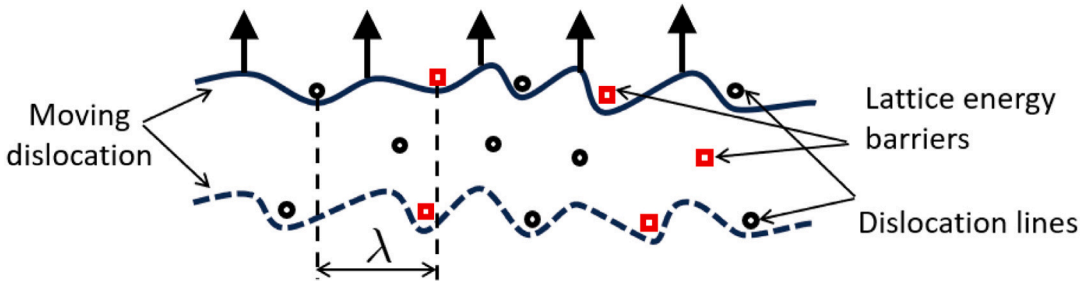

Fig. 5. A moving dislocation in the proposed scale bridging model. The dislocation motion is characterized by two contributions of the mean free path (see Eq. (21)). First contribution is defined by the lattice energy barriers (red squares) calculated by the atomistic random alloy model, and the second contribution is defined by the dislocation density (black circles).

mechanism is schematically represented in Fig. 5 where two contributions are possible. The contribution of lattice distortions barriers, as calculated by the random alloy model, is addressed in this section, while the second contribution due to dislocation density is detailed in the next sections.

In the literature, there are energy values reported for different mechanisms that can act as barriers during plastic deformation. For this, we need to consider all the possible defects in the crystal lattice which can act as barriers for dislocation motion. These include, the dislocation energy [50–52], the energy of the dislocation core [54,55], the vacancy migration energy [18], dislocation self climb activation energy [132] or the cross-slip energy [8]. Each of the listed structural defects has range of corresponding energies and be associated with local lattice distortions (Fig. 1). We chose the energy value, E_{act} = 2.27 eV, in the range 2–2.5 eV which is in agreement with relevant mechanisms for dislocation line energy [54], kink-pair energy [56] and modelling of dislocation energy [50–52]. After choosing the integration limit in Eq. (4), E_{act}, based on relevant dislocation energy values found in the literature, we integrate to obtain the mean free path, $\lambda_{lattice}$. Finally, using the method by Nohring and Curtin [8], for a chosen value of activation energy E_{act} = 2.27 eV, we can find the distance between barriers:

$$\frac{2 \cdot \sqrt{\frac{3}{2}} a_{lattice}}{0.1488 \cdot \int_{-2.27}^{\infty} e^{-\frac{1}{2} \cdot \frac{(E+2.748)^2}{0.27}} dE} \approx 200 \text{ nm} \tag{22}$$

where the lattice parameter of the alloy $a_{lattice}$ is taken from [129]. Thus, given the size of our cluster it can be said that the distance between the energy barriers is approximately 200 nm. All the parameters in (5) are within ranges reported in the literature. The calculated MFP is sensitive to the chosen value of each parameter employed in the random alloy model.

Although slightly different values of activation energy E_{act} are possible to define the integration limits in Eq. (22), we estimate the effect of other parameters in the atomistic model to have impact on the calculated mean free path. In particular, a much greater influence of the results (Eq. (4)) obtained by the random alloy model is influenced by the type of pair potential (and its parameters), the rules for obtaining mixed components and the value of lattice parameter, $a_{lattice}$, which is not trivial in the case of multicomponent alloys.

Our goal is the connection between structural properties and mechanical properties. The typical design of multi-component solid solutions involves thermodynamic approaches, such as the Hume-Rothery rules (e.g. similar atomic radii). These methods rely on Maxwell relations to calculated the averaged free energy and material properties (e.g. ThermoCalc or Calphad). But such approaches do not allow the full description of the structural properties and the associated free energy. A major challenge for the full (atomistic) description of the free energy of the HEA is the calculation of the configuration entropy. This can have a significant impact on the mechanical properties. While the first term in Eq. (1) defines the potential energy of the alloy, the second term defines the configuration entropy of the alloy, which depends on probabilities of atomic occupation in the HEA distorted lattice. The small differences (Hume-Rothery rules) between the chosen atomic sizes leads to an increase of the possible local configurations, and an increase of the configuration entropy term. This add complexity when calculating the free energy. For this reason we chose our atomic approach, even without direct calculation of the configuration entropy (Eq. (1)). In the next sections, the above considerations in the atomistic model will be bridged in the scales through mean free path considerations and dislocation theory.

4.2. Mesoscale model parameters and stress–strain curves

As presented earlier, our method combines atomistic and dislocation theory. The interaction between these methods provides a description of macro-level properties. Fig. 6 shows that the model can successfully predict the experimental stress–strain curves at two different temperatures [86] for most levels of strain. The dislocation theory model has been implemented by using parameters found in the literature or estimated from experiments. The model is sensitive to temperature and strain rate, although we only investigate the effect of the former in this study. The shear modulus G, b and their dependencies of temperature have been previously experimentally measured for this alloy [86]. The initial dislocation density is also used as an input for the model and it has been taken as the average of experimental observations [86, 133]. The Debye frequency is taken from experimentally validated calculations based on dislocation theory [95]. The activation energy for dislocation glide [94] is taken from the literature for this alloy (363 kJ/mol) [134]. The choice of A and B parameters has been chosen to fit the experimental stress–strain curves by using a Lipschitz condition algorithm. The obtained A and B parameters are consistent with theoretical ranges ($\approx 10^8$–10^9 s m^{-1} and $\approx$ 10–10^2 s) [109], when the slope of the stress hardening is approximated to $\approx G/200$ [85] and the reference hardening stress is taken as 426 MPa, which is the shear strength at 0 K (Pierls stress) for this alloy [135]. Our approached based on dislocation theory, along with these defined parameters, allow the calculation of mechanical properties which are temperature and strain-rate dependent.

As we are considering deformation at the bulk scale, most dislocations will be inside grains or relatively away ($\gtrsim 100b$) from the grain boundaries. Furthermore, because we can neglect grain boundary sliding at the studied relatively low temperatures, we expect a relatively high ratio of mobile-to-immobile (>1) dislocation density. We have explored which value of R = 1,5,10,20, and corresponding adjusted values of A and B, best fit the experimental dislocation density and flow curves. For each explored value of R, the adjusted values of A and B are within the theoretical limits ($\approx 10^8$–10^9 s m^{-1} and $\approx$ 10–10^2 s). Although all of these combinations of values of R, A and B generally give a reasonable agreement with the experimental flow curves and dislocation density (not shown), we found that R = 10 and the values of A and B as shown in 1 best match the experimental data. The accuracy

Table 1
Initial parameters employed in the present model to describe the plastic behaviour. All these values have a physical meaning and thus not arbitrarily chosen, as described in the main text. The values for all these parameters are constant for all model simulations.

$\lambda_{lattice}$ [m]	ρ_{to}^{0} [m^{-2}]	A [s m^{-1}]	B [s]	G_{77K} [GPa]	G_{293K} [GPa]	ν_D [s^{-1}]	Q [kJ/mole]	b [m]
$2 \cdot 10^{-7}$	$1.7 \cdot 10^{13}$	$2.7 \cdot 10^{8}$	50	85	80	10^{13}	363	$2.5 \cdot 10^{-10}$

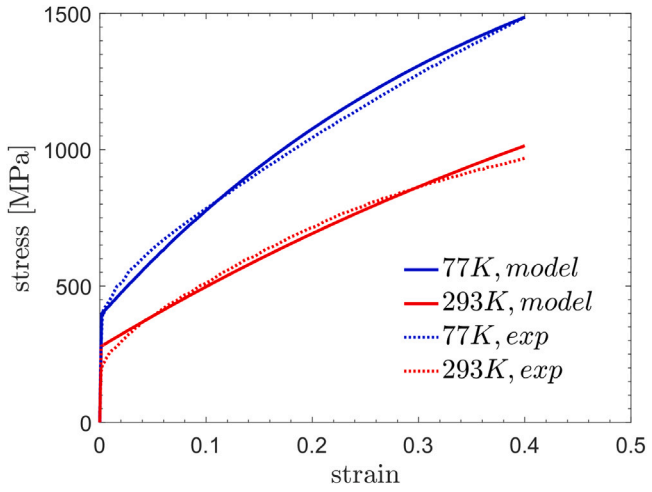

Fig. 6. Flow curves predictions at $\dot{\epsilon} = 10^{-4}$ s^{-1} by the proposed coupled atomic-meso scale model for HEAs and its validation against experimental data [86].

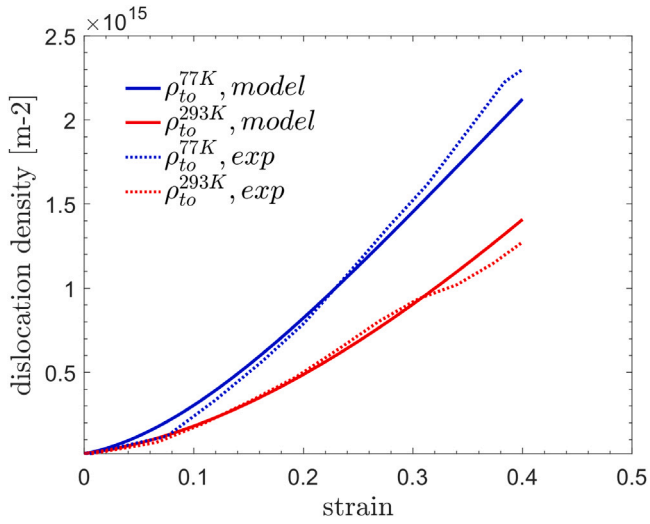

Fig. 7. Model calculations and experimentally determined dislocation densities in the studied HEA FeCrCoNi. [86,133]. The initial dislocation density is taken from the experimentally determined dislocation density before deformation, as $1.7 \cdot 10^{13}$ m^{-2} for both temperatures.

of the model could be improved in the early regions of plasticity $\epsilon < 0.5\%$ strain. The model predicts an abrupt change from elastic to plastic regime on the onset of yielding. This is a common behaviour of plastically deforming single crystals [117]. The model is effectively considering a single crystallographic orientation representing the average of the polycrystal via the Taylor factor [101]. This transition is much smoother when studying the response of the RVEs using the CPFEM framework [73,136–138], which is not captured by our simplified model. This smoother curve and a smoother transition into plasticity is a consequence of the aggregate of grains taking naturally into account the averaged effect of differently oriented grains, each with its own Schmidt factor, which is a determinant for plastic deformation. Moreover, CPFEM studies have demonstrated that elastic anisotropies can play an important role in the early stages of plasticity in FCC metals [64,68,69,139]. This can further explain the reason for the model not capturing the smoother elastic–plastic transition observed and predicted in polycrystals.

4.3. Evolution of the dislocation density

X-ray diffraction can be used to estimate the evolution of the total dislocation density. The broadening of diffraction peaks is often attributed to the presence of crystalline defects, including dislocations [140]. Both mobile and immobile dislocations in all slip systems, along with other crystalline defects, can contribute to the broadening of X-ray (or neutron) diffraction peaks. Thus, we can compare the predicted total dislocation density against the corresponding experimental data as determined by neutron diffraction for CrFeCoNi [86,133] is shown in Fig. 7. Overall, the model captures the trend of increase of the total dislocation density with strain. The magnitude of changes in dislocation density evolution following significant deformation ($\epsilon > 0.10$) are in agreement with general observations in other engineering metal alloys. The dislocation density can increase some orders of magnitude, from 10^{10} m^{-2} to 10^{11} m^{-2} in well annealed metals [117], to about 10^{14}–10^{15} m^{-2} in heavily cold-rolled metals [111]. Other modified K–M models have predicted similar evolution of dislocation density with strain in aluminium alloys [80] and nickel alloys [81]. The model predicts the increase of dislocation density to be less pronounced at higher strains ($\epsilon \gtrapprox 0.2$) for 77 K. This is noticeable by the crossing between the experimental and predicted dislocation densities for 77 K at about $\epsilon \approx 0.2$ strain. This suggests that the rate of increase in dislocation density with strain diminishes at these strains for 77 K, due to dynamic recovery (stage III hardening) as quantified by the dislocation annihilation term in Eq. (13).

Although the predictions by the model are generally in good agreement with the experimental observations for both temperatures, the model better predicts the dislocation density for strains below than $\epsilon \approx 0.3$. We attribute this difference to the combination of using an overly simplistic model and experimental data uncertainty. Firstly, our model is insensitive to other deformation mechanisms, such as twinning or micro-texture, and its effect on strain hardening. Furthermore, these mechanisms play different roles at different temperatures. For example, twinning is promoted at lower temperatures due the lower SFE. In the absence of twinning, deformation must be accommodated across the micro-structures, resulting in intragranular crystallographic texture changes. This is more significant near grain boundaries where the constraints imposed by the neighbouring grains are stronger [141]. Moreover, the overall crystallographic texture becomes more pronounced as strain increases and becomes significant strains ($\epsilon \gtrapprox 0.2$). In order to capture these effects on the strain hardening CPFEM models would be required. Secondly, one must be careful when interpreting the experimentally determined dislocation density. The dislocation density has been estimated from the peak broadening measurements around the diffraction angle for Bragg condition. Twining and micro-texture can also contribute to peak broadening in different amounts [86]. In this scenario, if twinning was to contribute significantly to peak broadening, the dislocation density would be experimentally overestimated, particularly at low temperatures where twining is more prominent. Additionally, other sources of experimental uncertainties can exist. For

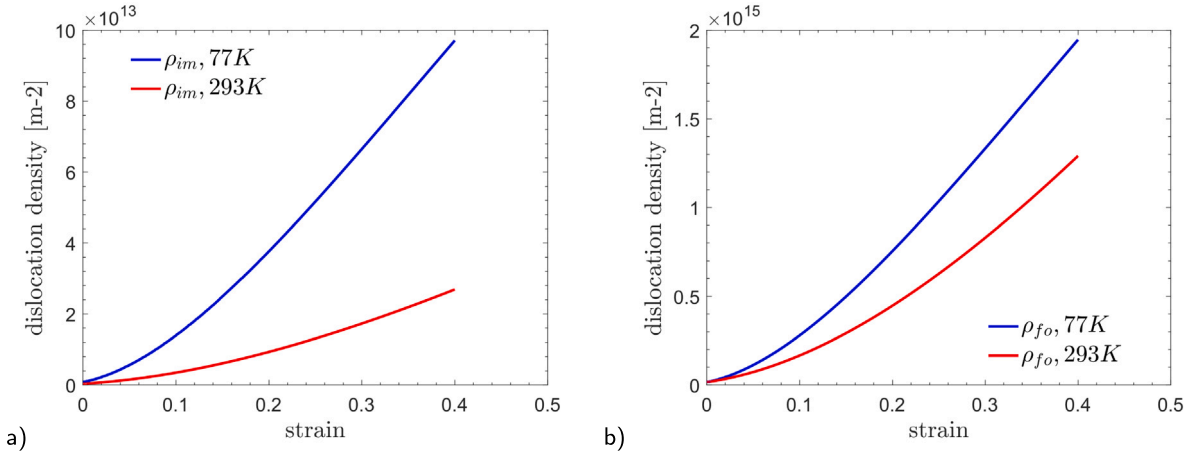

Fig. 8. Model predictions of the (a) immobile and the (b) forest dislocation densities for both temperatures in the studied FeCrCoNi alloy.

example, experimental determination of dislocation density from X-ray diffraction data often involves fitting the observed peak broadening to theoretical models, and various methods and corrections may be applied depending on the specifics of the material and experimental set-up. In conclusion, the predicted dislocation densities evolution with strain are in satisfactory agreement with the experimental data, given the possible contributions to uncertainties in the experimental data, and given the complexity of other deformation mechanisms which are not included in the constitutive behaviour of the model.

The evolution of the predicted immobile dislocation density is presented in Fig. 8a for both temperatures, 77 K (blue) and 293 K (red). The immobile dislocation density for 77 K rises steadily with the increase in strain, and almost linearly after about $\epsilon \approx 0.2$. Due to the effect of the higher stacking fault energy, and the corresponding increase in dislocation mobility, the immobile dislocation density is increasing more slowly at the higher temperature of 293 K than at 77 K for the same levels of strain. This reduced rate of increase in dislocation density at higher temperatures can be attributed to the ease with which dislocations can cross-slip or climb, bypassing obstacles more readily and thus extending the mean free path. In contrast, at the lower temperature of 77 K, the reduced stacking fault energy limits dislocation mobility, as reflected by the steeper blue curve. Here, dislocations are more likely to become immobile upon encountering obstacles, leading to a rapid accumulation of immobile dislocations and a consequent decrease in the mean free path. The larger immobile dislocation density during hardening at 77 K is responsible for the higher yield stress and the stronger response 6 than that at 293 K. This is explained by the lowering of the mean free path distance in the larger presence of immobile dislocations, which results in a higher resistance to dislocation movement.

The evolution of the forest dislocation density against strain for the two temperatures is depicted in 8b. As presented earlier, we assume the mean free path is unaffected by the forest dislocation density. Instead, the resistance to dislocation glide arises from the increased shear stress needed to overcome forest dislocations as given by the Taylor expression $\tau = \beta G b \sqrt{\rho_{fo}}$. The blue curve at 77 K, with its steeper increase in forest dislocation density, indicates a higher resistance to dislocation movement in the primary slip systems due to the frequent interactions with forest dislocations in the secondary systems. This increased interaction at the lower temperature results in a higher shear stress required to move dislocations, leading to greater material hardening and affecting the yield stress, as shown in Fig. 6. At 293 K, the red curve's more gradual slope suggests that the accumulation of forest dislocations is slower, thereby offering less resistance to dislocation movement in the primary slip systems. This results in a lower shear stress required for dislocation movement, hence a reduced hardening effect compared to the lower temperature condition. Comparing this to the immobile dislocation density in 8A, we observe that the accumulation of forest dislocations is significantly higher, as indicated by the scale of the y-axis. Despite this, the general trend remains the same, with the curve representing the lower temperature showing a greater rate of increase, emphasizing the increased shear stress resistance due to forest dislocations at lower temperatures. Finally, the chosen value of the mobile-to-immobile ratio (R) in Eq. (17) has a significant effect on the evolution of the immobile dislocation density (not shown). As presented earlier, we have chosen R = 10 because it best fits the experimental flow curves and total dislocation density. As expected, an decrease of R results in the immobile dislocation density increasing with respect to the mobile dislocation density for all levels of strain. On the other hand, the effect of changing R is much weaker for the results of forest dislocation density. This explained by the fact that the majority of dislocations are contained in secondary slip systems in the considered FCC lattice (Eq. (15)), acting therefore as forest dislocations regardless whether they are mobile or immobile.

4.4. Mean free path evolution

The dislocation mean free path evolution can be measured experimentally from microscopic images, although this is time consuming. There are several observable features that can contribute to the pinning of dislocations [25]. For example, individual contributions to the MFP have been reported, such as subgrains cells diameter [81] in aluminium alloys and or average twin spacing [119] in HEAs. In the proposed model, the atomistic approach is used to define the properties of the alloy structure in terms of the atomistic mean free path. As seen in previous sections, these calculations rely on the atomistic model for the stochastic calculation of lattice energy of HEAs and probability of energy barriers. This allows to obtain ground estimations of the evolution of the combined dislocation mean free path with strain. Here, we focus on the evolution of the mean free path in the primary slip system where deformation is being studied. The contributions to the combined mean free path (see Eq. (21)) arise from the atomistic mean free path and the mean free path determined by the immobile dislocations density in the given slip system, given by $\lambda = 1/\sqrt{\rho_{im}^{\alpha}}$. Fig. 9a shows the evolution of the combined mean free path at different temperatures. K–M models have predicted similar evolution of MFP with strain in aluminium alloys [80] and nickel alloys [81]. For both temperatures in Fig. 9a, the mean free path decreases with increasing strain, as expected. The blue curve, corresponding to a lower temperature of 77 K, starts at a lower mean free path when there is no strain. This is explained by the lower mobility of dislocations as shown in Eq. (19). As strain increases, the mean free path decreases, which means that

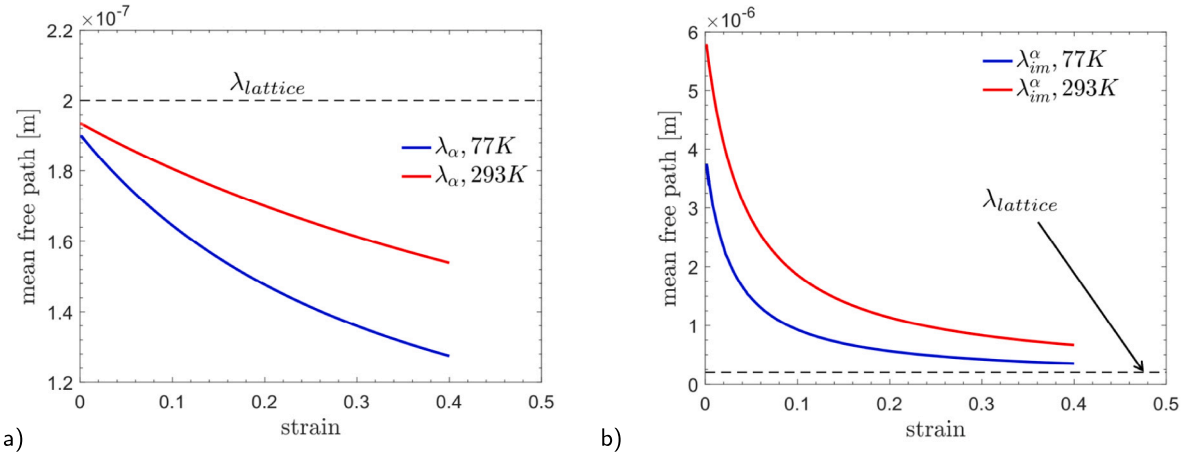

Fig. 9. Predicted evolution of the total mean free path (a) and the contribution of the immobile dislocation density to the mean free path (b). The mean free path represents the average distance between obstacles to dislocation motion in the primary slip system. The calculated contribution to the mean free path arising from lattice distortions in the HEA ($\lambda_{lattice}$), as predicted by the atomistic model, is shown as a dashed line.

the dislocations are encountering obstacles more frequently or that the obstacles are becoming more effective at impeding their movement. The red curve, representing the higher temperature of 293 K, begins with a higher mean free path at zero strain, indicating that dislocations can, on average, move a greater distance before being hindered by an obstacle. Therefore, that at lower temperatures, the dislocations can travel a shorter distance and become even more restricted with applied strain. At higher temperatures, dislocations start with more freedom of movement but still encounter increasing impediment from barriers as strain increases, although at a lesser rate than at lower temperatures.

As established in the Kocks–Mecking model used here, only the immobile dislocation density contributes to the combined mean free path in Eq. (21), not the forest dislocation density. However, the additional stress required to move forest dislocations included in the effective stress Eq. (10) via superimposes the drag stress via Eq. (11) and $\lambda = 1/\sqrt{\rho_{fo}}$. For this reason it we study the effective mean free path arising from forest dislocations in Fig. 9, which is calculated from the forest dislocation density. These include immobile dislocations in the current slip system as well as mobile dislocations on other slip systems. Forest dislocations oppose movement unless they cross slip, which is facilitated at higher temperatures and has been taken into account by means of the temperature dependent stacking fault energy. At zero strain, the mean free path is high for both temperatures, indicating a low initial dislocation density as determined experimentally. Without deformation, dislocations can travel relatively long distances without encountering forest dislocations. As strain increases, the mean free path decreases rapidly, reflecting an increase in forest dislocation density. More mobile dislocations are generated on other slip systems, which act as barriers and decrease the mean free path. The model predicts this decrease to be more pronounced at 77 K temperatures, explained by the rapid initial increase of dislocation density (mobile and immobile) in the previous section. At higher strains ($\gtrapprox$0.1) The convergence of the curves at higher strains suggests that the rate of increase in dislocation density with strain becomes more uniform at these strains for 77k, due to dynamic recovery processes as quantified by the dislocation annihilation term in equation Eq. (13). The rate at which the mean free path decreases diminishes, somewhat suggests a saturation where further increases in strain do not significantly alter the mean free path. Nevertheless, the experimental and predicted dislocation densities suggest that the mean free path will continue to decrease with strain, at least up to strains ≈40%.

The evolution of the mean free path calculated in Fig. 9 arising from the forest dislocation density indicates that, at strains $\gtrapprox$20%, the mean free path reaches significantly low values of ≈50 nm and lower.

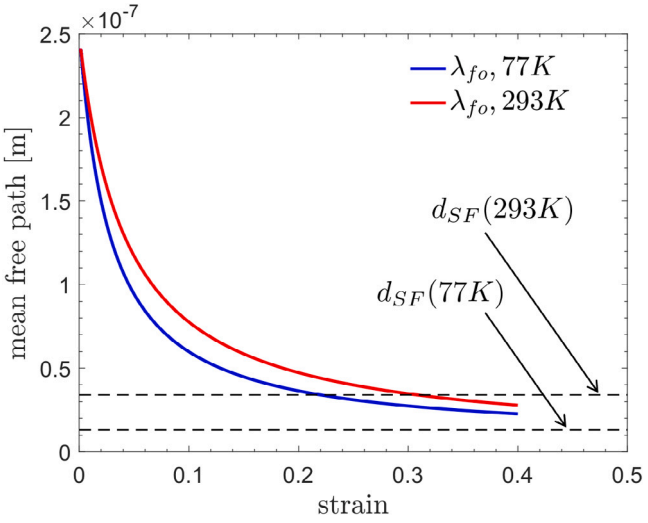

Fig. 10. Predicted evolution of the mean free path arising from forest dislocations. This mean free path arises from dislocations in secondary slip systems and results in a shear stress resistance to dislocation motion in the primary slip system. The calculated distances between partial dislocations for both temperatures are shown as dashed line.

These atomic distances are comparable to the typical distances between disassociated partial dislocations. Partial dislocations are segments of a complete dislocation that have separated, typically in fcc metals, leading to a stacking fault between them. This leads to a further interaction of dislocation movement of increased complexity from a strain hardening perspective. For example, stacking faults can block dislocations [142] or can react with dislocations by forming new obstacles, such as Lomer–Cottrell locks, which are immobile and contribute to the overall strength of the material. Furthermore, as the mean free path decreases, the ability for dislocations to cross slip (change slip planes) is reduced because the disassociated partial dislocations need to be associated before cross-slip [110], and the available space for such movement is constrained by the reduced mean free path. Cross slip is a mechanism that can relieve local stresses and allow dislocations to bypass obstacles, so its inhibition contributes to strain hardening. In general, these complex interactions become more likely when the mean free path is reduced, leading to a higher dislocation density within the proximity of partials. In 10, the calculated distances between partial dislocations for both studied temperatures are shown as horizontal

lines in the figure, and the corresponding calculation of distances is shown next. A fully associated dislocation with Burgers vector $b = a_{lattice}/2\langle 110\rangle$, tends to disassociate into Shockley partial dislocations with Burgers vectors of $a_{lattice}/6\langle 112\rangle$ directions due to energy minimization. Assuming elastic isotropy, the dissociation distance d can be approximated to the SFE, γ_{SFE}, via [111]:

$$d = \frac{Gb^2}{4\pi\gamma_{SFE}} \tag{23}$$

While these are approximated separation distances between partial dislocations, it is worth noting that a more precise calculation of the depends on the elastic anisotropy of the lattice, the dislocation characteristic and the actual Burgers vectors of Shockley partial dislocations [143]. In the context of HEAs, the spacing between partials has been calculated and measured as a function of the angle between the full dislocation and the Burgers vector [144]. The calculated separation distance showed some scatter and some variation with this angle, as expected from the theory. Here, our focus is merely to compare this approximated distance between Shockley partials with the mean free path, and to investigate the relevant mechanisms for dislocation barriers. When substituting with our γ^{77}_{SFE} and γ^{293}_{SFE}, we obtain a separation distance between Shockley partials of 13 nm and 34 nm respectively. The calculated distances are well below the mean free path at low strains and comparable to the MFP for strains beyond 0.3. In our approach we do not explicitly consider the effect of partial dislocations distance on glide in other slips systems, because the strain hardening arising from the sessile dislocations has already been accounted via the immobile dislocation density. It is, however, worth noting the complexity of the strain hardening phenomenon and the need for lower scale models, such as molecular dynamics, when investigating details related to stacking faults.

5. Conclusions

A scale-bridging physically-based model has been proposed for the mechanical properties estimation of a multicomponent alloy by statistically bridging the atomistic, dislocation and macro length scales. In the present model it has been assumed that the energy barriers act as pinning points for the movement of dislocations. The use of model potentials, to estimate the probability of occurrence of high energy barriers (2 eV), allowed us to calculate the dislocation mean free path distance, which is the average distance between obstacles opposing the dislocation motion. It has been here proposed a dislocation-based model where the dislocation motion is partially controlled by the mean free path distance calculated from our atomistic studies. In our model, the mean free path distance is also controlled by the dislocation density, which evolves according to a classic Kocks–Mecking expression. Concluding, the following considerations can be drawn:

- The assumptions of a linear relationship between the increase of SFE with the ratio of mobile-to-immobile dislocation densities and a linear relationship with temperature permit to obtain results consistent with experimental observations.
- The results show that our scale-bridging approach is able to capture the mean free path in the range of experimentally observed for other metals (50–200 nm). Further, the model is able to successfully predict experimentally-consistent dislocation density evolutions and flow curves.
- Although our methodology and results bring promise for the efficient design of HEAs, it is anticipated that further model validation would be needed for a wider range of HEA constituent elements, strain rates and temperatures.

CRediT authorship contribution statement

David Gonzalez: Writing – original draft, Validation, Methodology, Investigation, Formal analysis, Conceptualization. **Eugene Pavlov:** Writing – original draft, Investigation, Formal analysis, Conceptualization. **Stefano Valvano:** Writing – review & editing, Supervision. **Angelo Maligno:** Supervision, Funding acquisition.

Declaration of competing interest

The authors declare that they have no known competing financial interests or personal relationships that could have appeared to influence the work reported in this paper.

Acknowledgment

The research leading to these results has received funding from the European Union's Horizon 2020 research and innovation program under grant agreement no. 101004172 (ATLAS, Advanced Design of High Entropy Alloys Based Materials for Space Propulsion)

Data availability

Data will be made available on request.

References

[1] M A Hemphill, T Yuan, G Y Wang, J W Yeh, C W Tsai, A Chuang, P K Liaw, Fatigue behavior of Al 0.5 CoCrCuFeNi high entropy alloys, Acta Mater. (2012) http://dx.doi.org/10.1016/j.actamat.2012.06.046.

[2] Yanzhong Tian, Linlin Li, Jingjing Li, Yang Yang, Song Li, Gaowu Qin, Correlating strength and hardness of high-entropy alloys, Adv. Eng. Mater. (ISSN: 15272648) 23 (8) (2021) http://dx.doi.org/10.1002/adem.202001514.

[3] F. Otto, A. Dlouhý, Ch. Somsen, H. Bei, G. Eggeler, E.P. George, The influences of temperature and microstructure on the tensile properties of a CoCrFeMnNi high-entropy alloy, Acta Mater. (2013) 5743–5755.

[4] Cheng Lin, Yonggang Yao, Corrosion-resistant coating based on high-entropy alloys, Metals (ISSN: 20754701) 13 (2) (2023) http://dx.doi.org/10.3390/met13020205.

[5] Young Kyun Kim, Ka Ram Lim, Kee Ahn Lee, Superior resistance to high–temperature creep in an additively manufactured precipitation–hardened CrMnFeCoNi high–entropy alloy nanocomposite, Mater. Des. (ISSN: 18734197) 227 (2023) http://dx.doi.org/10.1016/j.matdes.2023.111761.

[6] Junjie Wang, Shangshu Wu, Shu Fu, Sinan Liu, Mengyang Yan, Qingquan Lai, Si Lan, Horst Hahn, Tao Feng, Ultrahigh hardness with exceptional thermal stability of a nanocrystalline CoCrFeNiMn high-entropy alloy prepared by inert gas condensation, Scr. Mater. (ISSN: 13596462) 187 (2020) 335–339, http://dx.doi.org/10.1016/j.scriptamat.2020.06.042.

[7] Y. Cheng, P. Liaw, Y. Zhang, T. Zuo, High-entropy alloys with high saturation magnetization, electrical resistivity and malleability, Sci. Rep. 3 (2013) 1–7.

[8] Wolfram Georg Nöhring, W.A. Curtin, Dislocation cross-slip in fcc solid solution alloys, Acta Mater. (ISSN: 13596454) 128 (2017) 135–148, http://dx.doi.org/10.1016/j.actamat.2017.02.027.

[9] Modupeola Dada, Patricia Popoola, Samson Adeosun, Ntombi Mathe, High entropy alloys for aerospace applications, in: Aerodynamics, 2021, http://dx.doi.org/10.5772/intechopen.84982.

[10] Bernd Gludovatz, Anton Hohenwarter, Dhiraj Catoor, Edwin H. Chang, Easo P. George, Robert O. Ritchie, A fracture-resistant high-entropy alloy for cryogenic applications, Science (ISSN: 10959203) 345 (6201) (2014) 1153–1158, http://dx.doi.org/10.1126/SCIENCE.1254581/SUPPL_FILE/GLUDOVATZ.SM.PDF, URL https://www.science.org/doi/10.1126/science.1254581.

[11] E.J. Pickering, N.G. Jones, High-entropy alloys: a critical assessment of their founding principles and future prospects, Int. Mater. Rev. 61 (3) (2016) 183–202.

[12] Jien Wei Yeh, Alloy design strategies and future trends in high-entropy alloys, JOM (ISSN: 10474838) 65 (12) (2013) 1759–1771, http://dx.doi.org/10.1007/s11837-013-0761-6.

[13] X. Yang, Y. Zhang, Prediction of high-entropy stabilized solid-solution in multi-component alloys, Mater. Chem. Phys. (ISSN: 02540584) 132 (2–3) (2012) 233–238, http://dx.doi.org/10.1016/j.matchemphys.2011.11.021.

[14] E.J. Pickering, N.G. Jones, High-entropy alloys: a critical assessment of their founding principles and future prospects, Int. Mater. Rev. (ISSN: 17432804) 61 (3) (2016) 183–202, http://dx.doi.org/10.1080/09506608.2016.1180020.

[15] Qingwei Guo, Xiaotao Xu, Xiaolong Pei, Zhiqiang Duan, Peter K Liaw, Hua Hou, Yuhong Zhao, Predict the phase formation of high-entropy alloys by compositions, J. Mater. Res. Technol. (2022) http://dx.doi.org/10.1016/j.jmrt.2022.12.143.

[16] Swati Singh, Nirmal Kumar Katiyar, Saurav Goel, Shrikrishna N Joshi, Phase prediction and experimental realisation of a new high entropy alloy using machine learning, Sci. Rep. 13 (4811) (2023) 123, http://dx.doi.org/10.1038/s41598-023-31461-7,

[17] Yaohua Gong, Tao Huang, Xun'An Zhang, Yongyong Suo, Purong Jia, Shuyi Zhao, Multiscale analysis of mechanical properties of 3d orthogonal woven composites with randomly distributed voids, Materials (ISSN: 19961944) 14 (18) (2021) http://dx.doi.org/10.3390/ma14185247.

[18] Won Mi Choi, Yong Hee Jo, Seok Su Sohn, Sunghak Lee, Byeong Joo Lee, Understanding the physical metallurgy of the CoCrFeMnNi high-entropy alloy: An atomistic simulation study, npj Comput. Mater. (ISSN: 20573960) 4 (1) (2018) http://dx.doi.org/10.1038/s41524-017-0060-9.

[19] Albert R. Khalikov, Evgeny A. Sharapov, Vener A. Valitov, Elvina V. Galieva, Elena A. Korznikova, Sergey V. Dmitriev, Simulation of diffusion bonding of different heat resistant nickel-base alloys, Computation (ISSN: 20793197) 8 (4) (2020) 1–12, http://dx.doi.org/10.3390/computation8040102.

[20] Bohayra Mortazavi, Mohammad Silani, Evgeny V. Podryabinkin, Timon Rabczuk, Xiaoying Zhuang, Alexander V. Shapeev, First-principles multiscale modeling of mechanical properties in graphene/borophene heterostructures empowered by machine-learning interatomic potentials, Adv. Mater. (ISSN: 15214095) 33 (35) (2021) http://dx.doi.org/10.1002/adma.202102807.

[21] Hsiao Wei Lee, Cemal Basaran, Predicting high cycle fatigue life with unified mechanics theory, Mech. Mater. (ISSN: 01676636) 164 (2022) http://dx.doi.org/10.1016/j.mechmat.2021.104116.

[22] Christopher Tandoc, Yong Jie Hu, Liang Qi, Peter K. Liaw, Mining of lattice distortion, strength, and intrinsic ductility of refractory high entropy alloys, npj Comput. Mater. (ISSN: 20573960) 9 (1) (2023) http://dx.doi.org/10.1038/s41524-023-00993-x.

[23] Yingying Wang, Jundong Wang, Mingqi Lei, Yao Yao, A crystal plasticity coupled damage constitutive model of high entropy alloys at high temperature, Acta Mech. Sin. (ISSN: 16143116) 38 (11) (2022) http://dx.doi.org/10.1007/s10409-022-22116-x.

[24] Xiaochong Lu, Jianfeng Zhao, Chao Yu, Zhiming Li, Qianhua Kan, Guozheng Kang, Xu Zhang, Cyclic plasticity of an interstitial high-entropy alloy: experiments, crystal plasticity modeling, and simulations, J. Mech. Phys. Solids (ISSN: 00225096) 142 (2020) http://dx.doi.org/10.1016/j.jmps.2020.103971.

[25] M. Fisk, J.C. Ion, L.E. Lindgren, Flow stress model for IN718 accounting for evolution of strengthening precipitates during thermal treatment, Comput. Mater. Sci. (2014) 531–539.

[26] Ed J. Pickering, Alexander W. Carruthers, Paul J. Barron, Simon C. Middleburgh, David E.J. Armstrong, Amy S. Gandy, High-entropy alloys for advanced nuclear applications, Entropy (ISSN: 10994300) 23 (1) (2021) 1–28, http://dx.doi.org/10.3390/e23010098.

[27] D. Bacon, D. Hull, Introduction to dislocations, 2001, http://dx.doi.org/10.1016/b978-0-7506-4681-9.x5000-7, ISBN 978-0-7506-4681-9.

[28] Prashant Singh, A.V. Smirnov, D.D. Johnson, Atomic short-range order and incipient long-range order in high-entropy alloys, Phys. Rev. B (ISSN: 1550235X) 91 (22) (2015) http://dx.doi.org/10.1103/PhysRevB.91.224204.

[29] Xuefei Chen, Qi Wang, Zhiying Cheng, Mingliu Zhu, Hao Zhou, Ping Jiang, Lingling Zhou, Qiqi Xue, Fuping Yuan, Jing Zhu, Xiaolei Wu, En Ma, Direct observation of chemical short-range order in a medium-entropy alloy, Nature (ISSN: 14764687) 592 (7856) (2021) 712–716, http://dx.doi.org/10.1038/s41586-021-03428-z.

[30] Y. Rao, W.A. Curtin, Analytical models of short-range order in FCC and BCC alloys, Acta Mater. (ISSN: 13596454) 226 (2022) http://dx.doi.org/10.1016/j.actamat.2022.117621.

[31] A. Khachaturyan, Theory of Structural Transformations in Solids, John Willey and Sons, 1983, p. 574.

[32] A. Smirnov, Molekulyarno-Kineticheskaya Teoriya Metallov, Nauka, 1966.

[33] Yan Ping Wang, Bang Sheng Li, Heng Zhi Fu, Solid solution or intermetallics in a high-entropy alloy, Adv. Eng. Mater. (ISSN: 14381656) 11 (8) (2009) 641–644, http://dx.doi.org/10.1002/adem.200900057.

[34] Z. Wu, H. Bei, F. Otto, G.M. Pharr, E.P. George, Recovery, recrystallization, grain growth and phase stability of a family of FCC-structured multi-component equiatomic solid solution alloys, Intermetallics (ISSN: 09669795) 46 (2014) 131–140, http://dx.doi.org/10.1016/j.intermet.2013.10.024.

[35] B. Gelchinskii, A. Rempel, High-entropy alloys: preparation, properties and practical application, Izvestiya. Ferr. Metall. 63 (3–4) (2020) 248–253.

[36] J.M. Cowley, An approximate theory of order in alloys, Phys. Rev. (ISSN: 0031899X) 77 (5) (1950) 669–675, http://dx.doi.org/10.1103/PhysRev.77.669.

[37] J.M. Cowley, Short- and long-range order parameters in disordered solid solutions, Phys. Rev. (ISSN: 0031899X) 120 (5) (1960) 1648–1657, http://dx.doi.org/10.1103/PhysRev.120.1648.

[38] W. Harrison, Pseudopotentiais in the Theory of Metals, Benjamin, 1966, p. 336.

[39] NIST, Interatomic potentials repository, NIST URL https://www.ctcms.nist.gov/potentials/.

[40] A. Dlouhý, R. Gröger, V. Vitek, Effective pair potential for random fcc CoCrFeMnNi alloys, Modelling Simul. Mater. Sci. Eng. 28 (7) (2020).

[41] David W. Jacobson, Gregory B. Thompson, Revisting lennard jones, morse, and N-M potentials for metals, Comput. Mater. Sci. (ISSN: 09270256) 205 (2022) http://dx.doi.org/10.1016/j.commatsci.2022.111206.

[42] Enrico Benassi, The Zero Point Position in Morse's potential and accurate prediction of thermal expansion in metals, Chem. Phys. (2018) http://dx.doi.org/10.1016/j.chemphys.2018.09.005.

[43] Li Yang, Lei Sun, Wei Qiao Deng, Combination rules for Morse-based van der Waals force fields, J. Phys. Chem. A (ISSN: 15205215) 122 (6) (2018) 1672–1677, http://dx.doi.org/10.1021/acs.jpca.7b11252, URL https://pubs.acs.org/doi/abs/10.1021/acs.jpca.7b11252.

[44] N.G. Jones, J.W. Aveson, A. Bhowmik, B.D. Conduit, H.J. Stone, On the entropic stabilisation of an Al0.5CrFeCoNiCu high entropy alloy, Intermetallics (ISSN: 09669795) 54 (2014) 148–153, http://dx.doi.org/10.1016/j.intermet.2014.06.004.

[45] N.G. Jones, K.A. Christofidou, H.J. Stone, Rapid precipitation in an Al0.5CrFeCoNiCu high entropy alloy, Mater. Sci. Technol. (U.K.) (ISSN: 17432847) 31 (10) (2015) 1171–1177, http://dx.doi.org/10.1179/1743284715Y.0000000004.

[46] E.J. Pickering, H.J. Stone, N.G. Jones, Fine-scale precipitation in the high-entropy alloy Al0.5CrFeCoNiCu, Mater. Sci. Eng. A (ISSN: 09215093) 645 (2015) 65–71, http://dx.doi.org/10.1016/j.msea.2015.08.010.

[47] X.D. Xu, P. Liu, S. Guo, A. Hirata, T. Fujita, T.G. Nieh, C.T. Liu, M.W. Chen, Nanoscale phase separation in a fcc-based CoCrCuFeNiAl0.5 high-entropy alloy, Acta Mater. (ISSN: 13596454) 84 (2015) 145–152, http://dx.doi.org/10.1016/j.actamat.2014.10.033.

[48] Interatomic spacing distribution in multicomponent alloys, Acta Mater. (ISSN: 13596454) 97 (2015) 156–169, http://dx.doi.org/10.1016/j.actamat.2015.07.010.

[49] Hui Feng, Jingwen Tang, Haotian Chen, Yuanyuan Tian, Qihong Fang, Jia Li, Feng Liu, Indentation-induced plastic behaviour of nanotwinned Cu/high entropy alloy FeCoCrNi nanolaminate: An atomic simulation, RSC Adv. (ISSN: 20462069) 10 (16) (2020) 9187–9192, http://dx.doi.org/10.1039/d0ra00518e.

[50] V. Kovalenko, G. Poletaev, Calculation of the energy of formation of edge, screw and twinning dislocations using the method of molecular dynamics, Basic Probl. Mater. Sci. (BPMS) 21 (1) (2023) 33–40, http://dx.doi.org/10.25712/ASTU.1811-1416.2023.01.004.

[51] Irina V. Zorya, Gennadii M. Poletaev, Roman Yu Rakitin, Energy and velocity of sliding of edge and screw dislocations in austenite and hadfield steel: Molecular dynamics simulation, Izvestiya Ferr. Metall. (ISSN: 24102091) 65 (12) (2022) 861–868, http://dx.doi.org/10.17073/0368-0797-2022-12-861-868.

[52] R.E. Kubilay, A. Ghafarollahi, F. Maresca, W.A. Curtin, High energy barriers for edge dislocation motion in body-centered cubic high entropy alloys, npj Comput. Mater. (ISSN: 20573960) 7 (1) (2021) http://dx.doi.org/10.1038/s41524-021-00577-7.

[53] N. Bertin, W. Cai, S. Aubry, V.V. Bulatov, Core energies of dislocations in bcc metals, Phys. Rev. Mater. (ISSN: 2475-9953) 5 (2021) 025002, http://dx.doi.org/10.1103/PhysRevMaterials.5.025002.

[54] X.W. Zhou, M.E. Foster, Character angle effects on dissociated dislocation core energy in aluminum, Phys. Chem. Chem. Phys. (ISSN: 14639076) 23 (5) (2021) 3290–3299, http://dx.doi.org/10.1039/d0cp05333c.

[55] D. Buey, L.G. Hector, M. Ghazisaeidi, Core structure and solute strengthening of second-order pyramidal c+a dislocations in Mg-Y alloys, Acta Mater. (ISSN: 13596454) 147 (2018) 1–9, http://dx.doi.org/10.1016/j.actamat.2017.12.066.

[56] Guillaume Hachet, Daniel Caillard, Lisa Ventelon, Emmanuel Clouet, Mobility of screw dislocation in BCC tungsten at high temperature in presence of carbon, Acta Mater. (ISSN: 13596454) 222 (2022) 117440, http://dx.doi.org/10.1016/j.actamat.2021.117440.

[57] Mulaine Shih, Jiashi Miao, Michael Mills, Maryam Ghazisaeidi, Stacking fault energy in concentrated alloys, Nature Commun. (ISSN: 2041-1723) 12 (2021) 3590, http://dx.doi.org/10.1038/s41467-021-23860-z.

[58] K.-Y. Tsai, M.-H. Tsai, J.-W. Yeh, Sluggish diffusion in Co–Cr–Fe–Mn–Ni high-entropy alloys, Acta Mater. (ISSN: 13596454) 61 (2013) 4887–4897, http://dx.doi.org/10.1016/j.actamat.2013.04.058.

[59] Mohammad Sajad Mehranpour, Hamed Shahmir, Mahmoud Nili-ahmadabadi, Precipitation kinetics in heavily deformed CoCrFeNiMn high entropy alloy, Mater. Lett. (ISSN: 0167577X) 288 (2021) 129359, http://dx.doi.org/10.1016/j.matlet.2021.129359.

[60] Xinran Zhou, Sicong He, Jaime Marian, Vacancy energetics and diffusivities in the equiatomic multielement Nb-Mo-Ta-W Alloy, Materials (ISSN: 1996-1944) 15 (2022) 5468, http://dx.doi.org/10.3390/ma15155468.

[61] J. Hure, S. El Shawish, L. Cizelj, B. Tanguy, Intergranular stress distributions in polycrystalline aggregates of irradiated stainless steel, J. Nucl. Mater. (ISSN: 0022-3115) 476 (2016) 231–242, http://dx.doi.org/10.1016/j.jnucmat.2016.04.017, URL https://www.sciencedirect.com/science/article/pii/S0022311516301313.

[62] D. Gonzalez, J.F. Kelleher, J. Quinta da Fonseca, P.J. Withers, Macro and Intergranular stress responses of austenitic stainless steel to 90° strain path changes, Mater. Sci. Eng. A 546 (2012) 263–271.

[63] Hamidreza Abdolvand, Marta Majkut, Jette Oddershede, Søren Schmidt, Ulrich Lienert, Bradley J. Diak, Philip J. Withers, Mark R. Daymond, On the deformation twinning of Mg AZ31b: A three-dimensional synchrotron X-ray diffraction experiment and crystal plasticity finite element model, Int. J. Plast. (ISSN: 0749-6419) 70 (2015) 77–97, http://dx.doi.org/10.1016/j.ijplas.2015.03.001, URL http://www.sciencedirect.com/science/article/pii/S0749641915000443.

[64] Jutian Chen, Junxia Lu, Wang Cai, Yuefei Zhang, Yongfeng Wang, Wenxiang Jiang, Muhammad Rizwan, Ze Zhang, In-situ study of adjacent grains slip transfer of Inconel 718 during tensile process at high temperature, Int. J. Plast. (ISSN: 0749-6419) 163 (2023) 103554, http://dx.doi.org/10.1016/j.ijplas.2023.103554, URL https://www.sciencedirect.com/science/article/pii/S0749641923000402.

[65] Van-Tung Phan, Xiang Zhang, Yumeng Li, Caglar Oskay, Microscale modeling of creep deformation and rupture in Nickel-based superalloy IN 617 at high temperature, Mech. Mater. (ISSN: 0167-6636) 114 (2017) http://dx.doi.org/10.1016/j.mechmat.2017.08.008, URL http://www.sciencedirect.com/science/article/pii/S016766361730265X.

[66] Markian P. Petkov, Elsiddig Elmukashfi, Edmund Tarleton, Alan C.F. Cocks, Evaluation of local stress state due to grain-boundary sliding during creep within a crystal plasticity finite element multi-scale framework, Int. J. Mech. Sci. 211 (2021) 106715, http://dx.doi.org/10.1016/J.IJMECSCI.2021.106715.

[67] Samir El Shawish, Leon Cizelj, Igor Simonovski, Modeling grain boundaries in polycrystals using cohesive elements: Qualitative and quantitative analysis, Nucl. Eng. Des. (ISSN: 0029-5493) 261 (2013) 371–381, http://dx.doi.org/10.1016/j.nucengdes.2013.01.023, URL https://www.sciencedirect.com/science/article/pii/S0029549313000460.

[68] D. Gonzalez, I. Simonovski, P.J. Withers, J. Quinta Da Fonseca, Modelling the effect of elastic and plastic anisotropies on stresses at grain boundaries, Int. J. Plast. 61 (2014) 49–63, http://dx.doi.org/10.1016/j.ijplas.2014.03.012.

[69] S. El Shawish, T. Mede, Grain boundary stresses in elastic materials, Eur. J. Mech. A Solids (ISSN: 0997-7538) 99 (2023) http://dx.doi.org/10.1016/j.euromechsol.2023.104940, URL https://www.sciencedirect.com/science/article/pii/S0997753823000323.

[70] Zhaojun Du, Keke Tang, Paolo Ferro, Quantitative analyses on geometric shape effect of microdefect on fatigue accumulation in 316L stainless steel, Eng. Fract. Mech. (ISSN: 0013-7944) 269 (2022) 108517, http://dx.doi.org/10.1016/j.engfracmech.2022.108517, URL https://www.sciencedirect.com/science/article/pii/S0013794422002569.

[71] Xiaoxian Zhang, Fionn P.E. Dunne, 3D CP-XFEM modelling of short crack propagation interacting with twist/tilt nickel grain boundaries, J. Mech. Phys. Solids (ISSN: 0022-5096) 168 (2022) 105028, http://dx.doi.org/10.1016/j.jmps.2022.105028, URL https://www.sciencedirect.com/science/article/pii/S0022509622002101.

[72] Umair Bin Asim, M. Amir Siddiq, Mehmet E. Kartal, A CPFEM based study to understand the void growth in high strength dual-phase titanium alloy (Ti-10V-2Fe-3Al), Int. J. Plast. (ISSN: 0749-6419) 122 (2019) 188–211, http://dx.doi.org/10.1016/j.ijplas.2019.07.002, URL https://www.sciencedirect.com/science/article/pii/S0749641919300105.

[73] Manas V. Upadhyay, Anirban Patra, Wei Wen, Tobias Panzner, Steven Van Petegem, Carlos N. Tomé, Ricardo A. Lebensohn, Helena Van Swygenhoven, Mechanical response of stainless steel subjected to biaxial load path changes: Cruciform experiments and multi-scale modeling, Int. J. Plast. (ISSN: 0749-6419) 108 (2018) 144–168, http://dx.doi.org/10.1016/j.ijplas.2018.05.003, URL https://www.sciencedirect.com/science/article/pii/S0749641917306046.

[74] Manas V. Upadhyay, Jan Capek, Tobias Panzner, Helena Van Swygenhoven, Microstructure evolution of stainless steel subjected to biaxial load path changes: In-situ neutron diffraction and multi-scale modeling, Int. J. Plast. (ISSN: 0749-6419) 122 (2019) 49–72, http://dx.doi.org/10.1016/j.ijplas.2019.06.006, URL https://www.sciencedirect.com/science/article/pii/S074964191830545X.

[75] D.M. Collins, T. Erinosho, F.P.E. Dunne, R.I. Todd, T. Connolley, M. Mostafavi, H. Kupfer, A.J. Wilkinson, A synchrotron X-ray diffraction study of non-proportional strain-path effects, Acta Mater. (ISSN: 1359-6454) 124 (2017) 290–304, http://dx.doi.org/10.1016/j.actamat.2016.11.011, URL http://www.sciencedirect.com/science/article/pii/S1359645416308734.

[76] Mengdi Li, Li Hu, Weijiu Huang, Xusheng Yang, Fei Guo, Effects of T1/T2 precipitates on deformation behavior and microstructure evolution of AA2099 Al–Li alloy: experimental investigation and crystal plasticity finite element modeling, J. Mater. Res. Technol. (ISSN: 2238-7854) 17 (2022) 342–352, http://dx.doi.org/10.1016/j.jmrt.2022.01.009, URL https://www.sciencedirect.com/science/article/pii/S2238785422000096.

[77] Chandrashekhar M. Pilgar, Ana M. Fernandez, Javier Segurado, Microstructure sensitive fatigue life prediction model for SLM fabricated Hastelloy-X, Int. J. Fatigue (ISSN: 0142-1123) 168 (2023) 107372, http://dx.doi.org/10.1016/j.ijfatigue.2022.107372, URL https://www.sciencedirect.com/science/article/pii/S0142112322006223.

[78] T.F.W. van Nuland, J.A.W. van Dommelen, M.G.D. Geers, Microstructural modeling of anisotropic plasticity in large scale additively manufactured 316L stainless steel, Mech. Mater. (ISSN: 0167-6636) 153 (2021) 103664, http://dx.doi.org/10.1016/j.mechmat.2020.103664, URL https://www.sciencedirect.com/science/article/pii/S0167663620306979.

[79] B. Attard, S. Cruchley, Ch. Beetz, M. Megahed, Y.L. Chiu, M.M. Attallah, Microstructural control during laser powder fusion to create graded microstructure Ni-superalloy components, Addit. Manuf. (ISSN: 2214-8604) 36 (2020) 101432, http://dx.doi.org/10.1016/j.addma.2020.101432, URL https://www.sciencedirect.com/science/article/pii/S2214860420308046.

[80] F. Barlat, M.V. Glazov, J.C. Brem, D.J. Lege, A simple model for dislocation behavior, strain and strain rate hardening evolution in deforming aluminum alloys, Int. J. Plast. (ISSN: 0749-6419) 18 (7) (2002) 919–939, http://dx.doi.org/10.1016/S0749-6419(01)00015-8, URL https://www.sciencedirect.com/science/article/pii/S0749641901000158.

[81] C. Keller, E. Hug, Kocks-Mecking analysis of the size effects on the mechanical behavior of nickel polycrystals, Int. J. Plast. (ISSN: 0749-6419) 98 (2017) 106–122, http://dx.doi.org/10.1016/j.ijplas.2017.07.003, URL https://www.sciencedirect.com/science/article/pii/S0749641917302620.

[82] David Gonzalez, ACF Cocks, Takuya Fukahori, Toshihide Igari, Yasuharu Chuman, Creep failure of a P91 simulated heat affected zone material under multiaxial state of stress, in: Proceedings of 3rd International ECCC Conference on Creep & Fracture, 2014.

[83] Rolf Sandström, Creep ductility, in: Basic Modeling and Theory of Creep of Metallic Materials, Springer, 2024, pp. 257–273.

[84] Hector Basoalto, Magnus Anderson, An extension of mean-field coarsening theory to include particle coalescence using nearest-neighbour functions, Acta Mater. 117 (2016) 122–134.

[85] H. Mecking, U.F. Kocks, Kinetics of flow and strain-hardening, Acta Metall. (ISSN: 0001-6160) 29 (11) (1981) 1865–1875, http://dx.doi.org/10.1016/0001-6160(81)90112-7, URL http://www.sciencedirect.com/science/article/pii/0001616081901127.

[86] Yiqiang Wang, Bin Liu, Kun Yan, Minshi Wang, Saurabh Kabra, Yu-Lung Chiu, David Dye, Peter D. Lee, Yong Liu, Biao Cai, Probing deformation mechanisms of a FeCoCrNi high-entropy alloy at 293 and 77K using in situ neutron diffraction, Acta Mater. (ISSN: 1359-6454) 154 (2018) 79–89, http://dx.doi.org/10.1016/j.actamat.2018.05.013, URL https://www.sciencedirect.com/science/article/pii/S1359645418303653.

[87] Abed Breidi, Joshua Allen, A. Mottura, First-principles calculations of intrinsic stacking fault energies and elastic properties in binary nickel alloys, Materialia (2024) 102080.

[88] Xiaoyang Zhang, Ruifeng Dong, Qingwei Guo, Hua Hou, Yuhong Zhao, Predicting the stacking fault energy in FCC high-entropy alloys based on data-driven machine learning, J. Mater. Res. Technol. (ISSN: 2238-7854) 26 (2023) 4813–4824, http://dx.doi.org/10.1016/j.jmrt.2023.08.194, URL https://www.sciencedirect.com/science/article/pii/S2238785423020070.

[89] Ho Conrad, Thermally activated deformation of metals, Jom 16 (1964) 582–588, Publisher: Springer.

[90] F.P.E. Dunne, D. Rugg, A. Walker, Lengthscale-dependent, elastically anisotropic, physically-based hcp crystal plasticity: Application to cold-dwell fatigue in Ti alloys, Int. J. Plast. (ISSN: 0749-6419) 23 (6) (2007) 1061–1083, http://dx.doi.org/10.1016/j.ijplas.2006.10.013, URL http://www.sciencedirect.com/science/article/pii/S0749641906001641, Number: 6.

[91] T. Suzuki, Y. Kamimura, H.O.K. Kirchner, Plastic homology of bcc metals, Phil. Mag. A (ISSN: 0141-8610) 79 (7) (1999) 1629–1642, http://dx.doi.org/10.1080/01418619908210383, Publisher: Taylor & Francis _eprint: https://doi.org/10.1080/01418619908210383.

[92] Shin Takeuchi, Tatsuo Hashimoto, Koji Maeda, Plastic deformation of bcc metal single crystals at very low temperatures, Trans. Japan Inst. Met. 23 (2) (1982) 60–69, http://dx.doi.org/10.2320/matertrans1960.23.60.

[93] Blazej Grabowski, Nikolay Zotov, Thermally-activated dislocation mobility in bcc metals: An accelerated molecular dynamics study, Comput. Mater. Sci. (ISSN: 0927-0256) 200 (2021) 110804, http://dx.doi.org/10.1016/j.commatsci.2021.110804, URL https://www.sciencedirect.com/science/article/pii/S0927025621005310.

[94] H.J. Frost, M.F. Ashby, Deformation-Mechanism Maps: the Plasticity and Creep of Metals and Ceramics, Pergamon Press, ISBN: 978-0-08-029338-7, 1982.

[95] U.F. Kocks, A.S. Argon, M.F. Ashby, Thermodynamics and Kinetics of Slip, in: Progress in materials science, Pergamon Press, ISBN: 978-0-08-017964-3, 1975, URL https://books.google.co.uk/books?id=B0AkMgEACAAJ.

[96] C. R Barrett, W.D. Nix, A model for steady state creep based on the motion of jogged screw dislocations, Acta Metall. (ISSN: 0001-6160) 13 (12) (1965) 1247–1258, http://dx.doi.org/10.1016/0001-6160(65)90034-9, URL http://www.sciencedirect.com/science/article/pii/0001616065900349.

[97] A.V. Granato, K. Lücke, J. Schlipf, L.J. Teutonico, Entropy factors for thermally activated unpinning of dislocations, J. Appl. Phys. (ISSN: 0021-8979) 35 (9) (1964) 2732–2745, http://dx.doi.org/10.1063/1.1713833.

[98] A. Seeger, Encyclopedia of Physics. Vol. VII, Part 1, Springerâ Verlag, Berlin, Germany, 1955.

[99] L. Kubin, J.L. Martin, Dislocations Ebookformation Plastique, Editions de physique, 1979, Google-Books-ID: fw6MxgEACAAJ.

[100] D. Caillard, J.L. Martin, Thermally Activated Mechanisms in Crystal Plasticity, Elsevier, ISBN: 978-0-08-054278-2, 2003, Google-Books-ID: VPbIvN7SkkcC.

[101] G.I. Taylor, The mechanism of plastic deformation of crystals. Part I.—Theoretical, Proc. R. Soc. Lond. Ser. A 145 (855) (1934) 362–387, http://dx.doi.org/10.1098/rspa.1934.0106, URL https://royalsocietypublishing.org/doi/10.1098/rspa.1934.0106.

[102] J. Friedel, Dislocations: International Series of Monographs on Solid State Physics, Elsevier, ISBN: 978-1-4831-3592-2, 1964, Google-Books-ID: c_kkBQAAQBAJ.

[103] M.F. Ashby, The deformation of plastically non-homogeneous materials, Phil. Mag. (ISSN: 1478-6435) 21 (170) (1970) 399, http://dx.doi.org/10.1080/14786437008238426.

[104] R. Madec, B. Devincre, L.P. Kubin, From dislocation junctions to forest hardening, Phys. Rev. Lett. 89 (25) (2002) 255508, http://dx.doi.org/10.1103/PhysRevLett.89.255508, URL https://link.aps.org/doi/10.1103/PhysRevLett.89.255508, Publisher: American Physical Society.

[105] A.J.E. Foreman, M.J. Makin, Dislocation movement through random arrays of obstacles, Philos. Mag.: J. Theor. Exp. Appl. Phys. (ISSN: 0031-8086) 14 (131) (1966) 911–924, http://dx.doi.org/10.1080/14786436608244762, URL https://www.tandfonline.com/doi/citedby/10.1080/14786436608244762, Publisher: Taylor & Francis.

[106] Alan Cottrell, Dislocations and Plastic Flow in Crystals, Clarendon Press, Oxford, 1953.

[107] U.F. Kocks, H. Mecking, Physics and phenomenology of strain hardening: the FCC case, Prog. Mater. Sci. (ISSN: 00796425) 48 (3) (2003) 171–273, http://dx.doi.org/10.1016/S0079-6425(02)00003-8, URL https://linkinghub.elsevier.com/retrieve/pii/S0079642502000038.

[108] J. Gil Gil-Sevillano, Paul Van Houtte, Etienne Aernoudt, Large strain work hardening and textures, Prog. Mater. Sci. 25 (2–4) (1980) 69–134, Publisher: Elsevier.

[109] Yuri Estrin, H. Mecking, A unified phenomenological description of work hardening based on one-parameter models, Acta Metall. 32 (1984) 57–70, http://dx.doi.org/10.1016/0001-6160(84)90202-5.

[110] John Price Hirth, Jens Lothe, Theory of Dislocations, second ed., Wiley Interscience, New York, ISBN: 978-0-471-09125-7, 1982, URL https://trove.nla.gov.au/version/45465590.

[111] Derek Hull, D.J. Bacon, Introduction to Dislocations, third ed., Butterworth-Heinemann, ISBN: 0-08-028720-4, 1984.

[112] Javier Gil Gil-Sevillano, Flow stress and work hardening, in: R.W. Cahn, P. Haasen, E.J. Kramer (Eds.), Material Science, Technology, first ed., Vol. 6, VCH Publishers Inc, Wiley, 1993, http://dx.doi.org/10.1002/9783527603978.mst0049, URL https://onlinelibrary.wiley.com/doi/10.1002/9783527603978.mst0049, ISBN 978-3-527-31395-2 978-3-527-60397-8.

[113] L.P. Kubin, Y. Estrin, Evolution of dislocation densities and the critical conditions for the Portevin-Le Chatelier effect, Acta Metall. Mater. (ISSN: 0956-7151) 38 (5) (1990) 697–708, http://dx.doi.org/10.1016/0956-7151(90)90021-8, URL https://www.sciencedirect.com/science/article/pii/0956715190900218.

[114] Alankar Alankar, Ioannis N. Mastorakos, David P. Field, A dislocation-density-based 3D crystal plasticity model for pure aluminum, Acta Mater. (ISSN: 1359-6454) 57 (19) (2009) 5936–5946, http://dx.doi.org/10.1016/j.actamat.2009.08.028, URL http://www.sciencedirect.com/science/article/pii/S1359645409005321.

[115] A.S. Argon, S. Takeuchi, Internal stresses in power-law creep, Acta Metall. (ISSN: 0001-6160) 29 (11) (1981) 1877–1884, http://dx.doi.org/10.1016/0001-6160(81)90113-9, URL https://www.sciencedirect.com/science/article/pii/0001616081901139.

[116] G. Gottstein, A.S. Argon, Dislocation theory of steady state deformation and its approach in creep and dynamic tests, Acta Metall. (ISSN: 0001-6160) 35 (6) (1987) 1261–1271, http://dx.doi.org/10.1016/0001-6160(87)90007-1, URL https://www.sciencedirect.com/science/article/pii/0001616087900071.

[117] Robert William Kerr Honeycombe, The plastic deformation of metals, 1984, ISBN 0-87170-186-3 978-0-87170-186-2.

[118] S.F. Liu, Y. Wu, H.T. Wang, J.Y. He, J.B. Liu, C.X. Chen, X.J. Liu, H. Wang, Z.P. Lu, Stacking fault energy of face-centered-cubic high entropy alloys, Intermetallics (ISSN: 0966-9795) 93 (2018) 269–273, http://dx.doi.org/10.1016/j.intermet.2017.10.004, URL https://www.sciencedirect.com/science/article/pii/S0966979517307379.

[119] G. Laplanche, A. Kostka, O.M. Horst, G. Eggeler, E.P. George, Microstructure evolution and critical stress for twinning in the CrMnFeCoNi high-entropy alloy, Acta Mater. (ISSN: 1359-6454) 118 (2016) 152–163, http://dx.doi.org/10.1016/j.actamat.2016.07.038, URL https://www.sciencedirect.com/science/article/pii/S1359645416305468.

[120] Farghalli A. Mohamed, Terence G. Langdon, The transition from dislocation climb to viscous glide in creep of solid solution alloys, Acta Metall. (ISSN: 0001-6160) 22 (6) (1974) 779–788, http://dx.doi.org/10.1016/0001-6160(74)90088-1, URL https://www.sciencedirect.com/science/article/pii/0001616074900881.

[121] A.S. Argon, W.C. Moffatt, Climb of extended edge dislocations, Acta Metall. (ISSN: 0001-6160) 29 (2) (1981) 293–299, http://dx.doi.org/10.1016/0001-6160(81)90156-5, URL https://www.sciencedirect.com/science/article/pii/0001616081901565.

[122] L. Rémy, A. Pineau, B. Thomas, Temperature dependence of stacking fault energy in close-packed metals and alloys, Mater. Sci. Eng. (ISSN: 0025-5416) 36 (1) (1978) 47–63, http://dx.doi.org/10.1016/0025-5416(78)90194-5, URL https://www.sciencedirect.com/science/article/pii/0025541678901945.

[123] Thomas Edward James Edwards, Fabio Di Gioacchino, Gaurav Mohanty, Juri Wehrs, Johann Michler, William John Clegg, Longitudinal twinning in a TiAl alloy at high temperature by in situ microcompression, Acta Mater. (ISSN: 1359-6454) 148 (2018) 202–215, http://dx.doi.org/10.1016/j.actamat.2018.01.007, URL https://www.sciencedirect.com/science/article/pii/S1359645418300387.

[124] E.P. Busso, F.T. Meissonnier, N.P. O'Dowd, Gradient-dependent deformation of two-phase single crystals, J. Mech. Phys. Solids (ISSN: 0022-5096) 48 (11) (2000) 2333–2361, http://dx.doi.org/10.1016/S0022-5096(00)00006-5, URL http://www.sciencedirect.com/science/article/B6TXB-410MG79-6/2/a91bdd0a4e70331a799cc37bf606b404.

[125] McDowell David L, Viscoplasticity of heterogeneous metallic materials, Mater. Sci. Eng. R (ISSN: 0927-796X) 62 (3) (2008) 67–123, http://dx.doi.org/10.1016/j.mser.2008.04.003, URL http://www.sciencedirect.com/science/article/pii/S0927796X08000430.

[126] Fabio Di Gioacchino, Joao Quinta da Fonseca, An experimental study of the polycrystalline plasticity of austenitic stainless steel, Int. J. Plast. (ISSN: 0749-6419) 74 (2015) 92–109, http://dx.doi.org/10.1016/j.ijplas.2015.05.012, URL https://www.sciencedirect.com/science/article/pii/S0749641915000820.

[127] Ainara Irastorza-Landa, Nicolò Grilli, Helena Van Swygenhoven, Effect of pre-existing immobile dislocations on the evolution of geometrically necessary dislocations during fatigue, Modelling Simul. Mater. Sci. Eng. (ISSN: 0965-0393) 25 (5) (2017) 055010, http://dx.doi.org/10.1088/1361-651X/aa6e24, Publisher: IOP Publishing.

[128] Daniel N. Blaschke, Abigail Hunter, Dean L. Preston, Analytic model of the remobilization of pinned glide dislocations: Including dislocation drag from phonon wind, Int. J. Plast. (ISSN: 0749-6419) 131 (2020) 102750, http://dx.doi.org/10.1016/j.ijplas.2020.102750, URL https://www.sciencedirect.com/science/article/pii/S0749641919309258.

[129] Biao Cai, Bin Liu, Saurabh Kabra, Yiqiang Wang, Kun Yan, Peter D Lee, Yong Liu, Deformation mechanisms of mo alloyed FeCoCrNi high entropy alloy: In situ neutron diffraction, Acta Mater. (2017) http://dx.doi.org/10.1016/j.actamat.2017.01.034.

[130] C. Kittel, Introduction to Solid State Physics, eightth ed., Wiley, 2005.

[131] Hualei Zhang, Xun Sun, Song Lu, Zhihua Dong, Xiangdong Ding, Yunzhi Wang, Levente Vitos, Elastic properties of AlxCrMnFeCoNi high-entropy alloys from ab initio theory, Acta Mater. (ISSN: 13596454) 155 (2018) 12–22, http://dx.doi.org/10.1016/j.actamat.2018.05.050.

[132] Thomas D. Swinburne, Kazuto Arakawa, Hirotaro Mori, Hidehiro Yasuda, Minoru Isshiki, Kouji Mimura, Masahito Uchikoshi, Sergei L. Dudarev, Fast, vacancy-free climb of prismatic dislocation loops in bcc metals, Sci. Rep. (ISSN: 20452322) 6 (2016) http://dx.doi.org/10.1038/srep30596.

[133] Muhammad Naeem, Haiyan He, Stefanus Harjo, Takuro Kawasaki, Weitong Lin, Ji-Jung Kai, Zhenduo Wu, Si Lan, Xun-Li Wang, Temperature-dependent hardening contributions in CrFeCoNi high-entropy alloy, Acta Mater. (ISSN: 1359-6454) 221 (2021) 117371, http://dx.doi.org/10.1016/j.actamat.2021.117371, URL https://www.sciencedirect.com/science/article/pii/S1359645421007503.

[134] K.A. Rozman, M. Detrois, M.C. Gao, P.D. Jablonski, J.A. Hawk, Long-term creep behavior of a CoCrFeNi medium-entropy alloy, J. Mater. Eng. Perform. 31 (11) (2022) 9220–9235, http://dx.doi.org/10.1007/s11665-022-06896-0, URL https://link.springer.com/10.1007/s11665-022-06896-0, ISSN 1059-9495, 1544-1024.

[135] Z. Wu, H. Bei, G.M. Pharr, E.P. George, Temperature dependence of the mechanical properties of equiatomic solid solution alloys with face-centered cubic crystal structures, Acta Mater. (ISSN: 1359-6454) 81 (2014) 428–441, http://dx.doi.org/10.1016/j.actamat.2014.08.026, URL https://www.sciencedirect.com/science/article/pii/S1359645414006272.

[136] Dylan Agius, Abdullah Al Mamun, Chris A. Simpson, Christopher Truman, Yiqiang Wang, Mahmoud Mostafavi, David Knowles, Microstructure-informed, predictive crystal plasticity finite element model of fatigue-dwells, Comput. Mater. Sci. (ISSN: 0927-0256) 183 (2020) 109823, http://dx.doi.org/10.1016/j.commatsci.2020.109823, URL https://www.sciencedirect.com/science/article/pii/S0927025620303141.

[137] Kai-Shang Li, Run-Zi Wang, Xian-Cheng Zhang, Shan-Tung Tu, Creep-fatigue damage mechanisms and life prediction based on crystal plasticity combined with grain boundary cavity model in a nickel-based superalloy at 650°C, Int. J. Plast. (2023) 103601.

[138] D. Gonzalez, A. King, I. Simonovski, J. Quinta da Fonseca, P.J. Withers, Modelling and measurement of plastic deformation and grain rotation in 3D at the grain-to-grain level, 2011, pp. 107–112, URL http://publications.jrc.ec.europa.eu/repository/handle/111111111/22753.

[139] M. Sauzay, Cubic elasticity and stress distribution at the free surface of polycrystals, Acta Mater. (ISSN: 1359-6454) 55 (4) (2007) 1193–1202, URL http://apps.isiknowledge.com/full_record.do?product=WOS&search_mode=GeneralSearch&qid=99&SID=R1JB2M1BjKED7lGaMGo&page=1&doc=5.

[140] G.K. Williamson, R.E. Smallman, III. dislocation densities in some annealed and cold-worked metals from measurements on the X-ray debye-scherrer spectrum, Philos. Mag.: J. Theor. Exp. Appl. Phys. (ISSN: 0031-8086) 1 (1) (1956) 34–46, http://dx.doi.org/10.1080/14786435608238074, Publisher: Taylor & Francis _eprint: https://doi.org/10.1080/14786435608238074.

[141] Shraddha J. Vachhani, Roger D. Doherty, Surya R. Kalidindi, Studies of Grain Boundary Regions in deformed polycrystalline aluminum using spherical nanoindentation, Int. J. Plast. (2016) 87–101.

[142] Haojie Wei, Yueguang Wei, Interaction between a screw dislocation and stacking faults in FCC metals, Mater. Sci. Eng. A (ISSN: 0921-5093) 541 (2012) 38–44, http://dx.doi.org/10.1016/j.msea.2012.01.115.

[143] D.J. Bacon, D.M. Barnett, R.O. Scattergood, Anisotropic continuum theory of lattice defects, Prog. Mater. Sci. (ISSN: 00796425) 23 (1980) 51–262, http://dx.doi.org/10.1016/0079-6425(80)90007-9, URL https://linkinghub.elsevier.com/retrieve/pii/0079642580900079.

[144] G. Laplanche, A. Kostka, C. Reinhart, J. Hunfeld, G. Eggeler, E.P. George, Reasons for the superior mechanical properties of medium-entropy CrCoNi compared to high-entropy CrMnFeCoNi, Acta Mater. (ISSN: 1359-6454) 128 (2017) 292–303, http://dx.doi.org/10.1016/j.actamat.2017.02.036, URL https://www.sciencedirect.com/science/article/pii/S135964541730126X.